UNIVERSITY OF GRONINGEN

BACHELOR THESIS

Voids and the Hubble tension issue

Author:
Emma Giovinazzo

Supervisor:
Prof. dr. Rien van de Weijgaert
Second examiner
prof. dr. Reynier Peletier

3 July 2020

Abstract

This thesis aims to explore how voids can contribute to the lack of uniformity in the measured Hubble constant (H_0) values. This will be done firstly by setting up a model with spherical voids, whose particles are given a peculiar velocity and analyzing the radial velocity - distance relation with observers both inside and outside voids. Next, the radial velocity - distance relation will be analyzed in a ΛCDM N-body simulation. There, the difference in inferred H_0 when observing from a void, filament, node, or wall will be investigated. Subsequently, dark matter halos will be identified from the ΛCDM simulation and the radial velocity - distance relation will once more be analyzed, with observers again in the same features.

Acknowledgements

I would first like to thank my supervisor Rien van de Weygaert for guiding and helping me through the project and sharing his knowledge on such an interesting topic.
I would also like to thank Roi Kugel and Bram Alferink for providing me with data without which this thesis would have barely existed.
Lastly, I would also like to thank Nidhi Bangera and Thijs van Beers for keeping me company and giving me emotional support.

Contents

1 Introduction **1**

2 FRWL Universe and the Hubble parameter **3**
2.1 Hubble parameter in FRWL cosmology 3
2.1.1 Proper definition 3
2.1.2 Friedmann equation and the Hubble parameter 4
2.2 Hubble Law 5
2.3 Hubble Tension 7
2.3.1 Methods for measuring H_0 9
2.3.2 Early Universe measurements 9
2.3.3 Late Universe measurements 11

3 Voids **13**
3.1 Spherical Model 15
3.1.1 Definitions 18
3.1.2 Shell Solutions 20
3.1.3 Density Evolution 22
3.1.4 Shell Velocities 22
3.1.5 Shell Crossing 23
3.2 Voids and the Hubble constant 24

4 Bubble Model **25**
4.1 Building the model 25
4.1.1 Void clustering 25
4.1.2 Creation of voids 26
4.1.3 Velocities 26
4.1.4 Representations 27
4.2 Method for taking lines of sight 31

5 Results of Bubble Model **32**
5.1 Various void clustering 35
5.2 Discussion on bubble model results 38

6 ΛCDM cosmology: Voids and the measured Hubble parameter 39
6.1 ΛCDM Model 39
6.2 N-body Simulation 40
6.3 MMF/Nexus 40
6.4 Dark matter 42
6.5 Dark matter halos 46
6.6 Method for taking lines of sight 47

7 Results of ΛCDM simulation 52
7.1 N-body Simulation 52
7.2 Dark matter halos 54
7.2.1 Selection of halos 55
7.3 Discussion on results of ΛCDM simulation 55

8 Conclusion and improvements 60
8.1 Conclusion 60
8.2 Comparison of results with literature 60
8.3 Improvements 61

Bibliography 63

Chapter 1

Introduction

The universe is expanding, it has been since the Big Bang, but how fast, exactly? Seems like a trivial question, but it is actually far from it.
The Hubble constant, discovered by Edwin Hubble in 1929, indicates how fast matter in the universe is moving away from each other due to the expansion of the universe. This constant is a fundamental tool in Astronomy, as it makes finding the distance to objects a trivial task, once their radial velocity is known. It is also extremely useful to determine the possible future of the universe (Panek, 2020).
Having a set value for the constant, with minimum uncertainty, is thus very important to accurately perform measurements.
The value of the Hubble constant has been calculated and refined many times since its discovery, using a variety of methods, such as using a cosmic distance ladder, calibrated from Cepheids and type Ia supernovae, to find the distance to objects whose velocity is known, or using the variations in temperature of the Cosmic Microwave Background, derived from the *Plack* data. At the moment of writing this thesis, the values found using different methods disagree with each other. The disagreement is quite a substantial one, about 3σ, a big enough difference that it might be due to something missing in our current understanding of the cosmos (Panek, 2020).
Something very interesting about this disagreement is that the CMB measurements from the *Planck* data appear to be a lower limit on all the other estimates, which might be another hint to the fact that there is something else at play and this disagreement does not only come from measuring errors.
There are many theories on why this discrepancy between the inferred values of the Hubble constant has occurred, but none of them has yet been proved to be correct. This thesis aims to investigate one of these theories, which involves the presence of voids.
Matter in voids expands in what is called a superHubble expansion, meaning that the matter not only moves due to the expansion of the universe but it also has its own peculiar velocity. This extra velocity is speculated to possibly affect the value of the calculated Hubble constant.

This possibility will be investigated first with a simple bubble model and then with a λCDM N-body simulation.
The bubble model is simply made up of "outside" points, with no peculiar velocity and bubbles of points with some peculiar velocity, which represent the voids. In this model lines of sight were taken both from inside and outside voids and the values of the inferred Hubble constants in those directions were analyzed.
The N-body simulation was instead probed with the NEXUS formalism to identify structures. Subsequently, lines of sight were taken from voids, filaments, walls and nodes, to analyze the difference in inferred Hubble constants.
Overall, what this thesis is trying to achieve is an analysis of what effect voids could have on the inferred Hubble constant calculated by an observer placed in different features of the cosmic web.

Chapter 2

FRWL Universe and the Hubble parameter

In this chapter, the importance of the Hubble parameter in the context of Friedmann-Robertson-Walker-Lemaître cosmology will be discussed.
First, the importance of the Hubble parameter and its relation with other cosmological factors will be introduced. Subsequently, Hubble law and its discovery will be discussed, to then move on to a history of the various values H_0 was though to have during the years, particularly focusing on the current Hubble tension. At the end of the chapters, the primary methods used to calculate H_0 will be explained.

2.1 Hubble parameter in FRWL cosmology

Before beginning the discussion about the role of the Hubble parameter in the FRLW cosmology it should be pointed out that "Hubble parameter" refers to the time-varying function H(t), whereas "Hubble constant" refers to H_0, which is the value of H(t) at the present day (Ryden, 2016).
The subscript 0 here, and in cosmology in general, indicates not the initial condition but the current condition.

2.1.1 Proper definition

The Hubble parameter is defined as

$$H(t) = \dot{a}/a \tag{2.1}$$

and the Hubble constant is:

$$H_0 = (\dot{a}/a)_{t=t_0} \tag{2.2}$$

where a(t) is the scale factor that relates the expansion of the universe with time (Ryden, 2016) and $\dot{a}$ is the time derivative of $a(t)$. The scale factor is unitless and at the present moment, which is $t = t_0$, it is defined to be 1. The existence of such expansion implies that everything was close together in the past, thus the observation of redshift leads naturally to the Big Bang model (Ryden, 2016). This is pretty clear, if everything is moving away from each other, everything had to be together at one point in time, in a singularity, which is the starting point of the Big Bang model. Assuming there are no forces that accelerate or decelerate the motion of galaxies, the time elapsed since any galaxies were together, which is the time elapsed since the Big Bang, can be found as (Ryden, 2016)

$$t_0 = \frac{r}{v} = \frac{r}{H_0 r} = H_0^{-1} \tag{2.3}$$

which is also known as Hubble time.

2.1.2 Friedmann equation and the Hubble parameter

The Hubble parameter can be tied to the Friedmann equation, a fundamental equation of cosmology as (Ryden, 2016):

$$H(t)^2 = \frac{8\pi G}{3c^2}\epsilon(t) - \frac{\kappa c^2}{R_0^2 a(t)^2} \tag{2.4}$$

where G is the gravitational constant, c is the speed of light, *a(t)* is the scale factor, R is the radius of curvature, $\epsilon(t)$ is the energy density and κ is the curvature constant. κ can only assume values of -1 for negatively curved space, 0 for flat space, and +1 for positively curved space.
Friedmann first derived this equation in 1922. It follows from Einstein's field equations and it describes how a spatially homogeneous and isotropic universe expands with time. This equation plays an essential role in Friedmann-Robertson-Walker-Lemaître, or FRWL, cosmology. FRWL cosmology is based on the assumption of isotropy and homogeneity, which is only true on very large scales, in the hundreds of Mpc, making it only an approximation. On smaller scales gravity holds matter together, making expansion not isotropic. However, on scales large enough the expansion of the universe can be treated as ideal, isotropic, and homogeneous and it can be described by a single scale factor $a(t)$ (Ryden, 2016).
At the present time, the Friedmann equation is (Ryden, 2016)

$$H_0^2 = \frac{8\pi G}{3c^2}\epsilon_0 - \frac{\kappa c^2}{R_0^2} \tag{2.5}$$

This equation thus gives a strong relation between H_0, which gives the current rate of expansion, ϵ_0 which gives the current energy density and κ/R_0^2. This means that if it was possible to know the precise value of H_0 and ϵ_0

it would be possible to also determine the radius of curvature, which is important to determine other qualities of the universe. Thus, having an precise value of H_0 is necessary for cosmology.
In a spatially flat universe, so with $\kappa = 0$ the Friedmann equation takes the form

$$H(t)^2 = \frac{8\pi G}{3c^2}\epsilon(t) \tag{2.6}$$

indicating that for a given value of $H(t)$ a critical density can be found from (Ryden, 2016)

$$\epsilon_c(t) = H(t)^2 \frac{3c^2}{8\pi G} \tag{2.7}$$

A value of $\epsilon(t) > \epsilon_c(t)$ indicates a positively curved universe whereas the opposite indicates a negatively curved universe.
When talking about density it is more useful to introduce the density parameter

$$\Omega(t) = \frac{\epsilon(t)}{\epsilon_c(t)} \tag{2.8}$$

which can also be used to rewrite the Friedmann equation to

$$1 - \Omega(t) = -\frac{\kappa c^2}{R_0^2 a(t)^2 H(t)^2} \tag{2.9}$$

This introduces an important relation between $\Omega(t)$ and $H(t)$, two very important quantities in cosmology.

2.2 Hubble Law

The Hubble law, or Hubble-Lemaître law (IAU) indicates the relation between the distance of an object to the observer and velocity at which it is moving away, due to the expansion of the universe. The Hubble law is simply

$$v = H_0 \times D \tag{2.10}$$

where v is the recession velocity (in km/s), D is the distance of the object from the observer (in Mpc) and H_0 is the Hubble constant (in km/s/Mpc).
The Hubble flow, which is evidence for the expansion of the universe, was discovered in 1929 by Edwin Hubble, who had surveyed the redshift of 50 galaxies to understand if a galaxy's redshift is dependent on the distance to the observer (Ryden, 2016). Unfortunately, measuring distances is much more difficult than measuring redshifts, thus he only estimated distances to 20 of them (Ryden, 2016). He then plotted these redshifts and distances, as seen in figure 2.1 and reached the relation

$$z = \frac{H_0}{c} r \tag{2.11}$$

If the redshifts are interpreted as Doppler shifts this relation takes the form seen in equation 2.10.

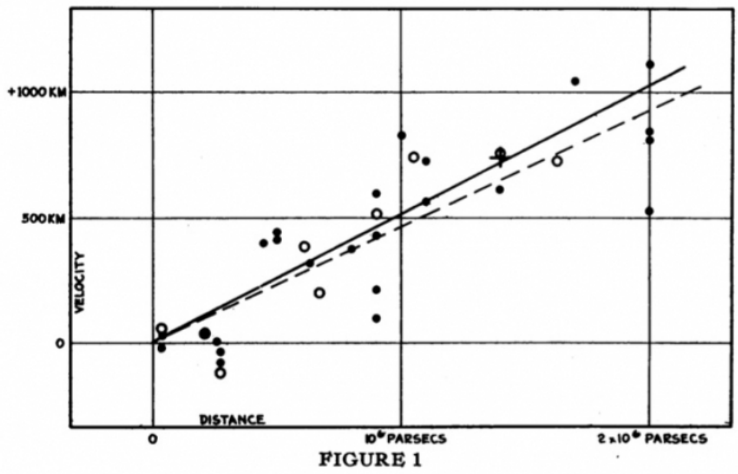

FIGURE 1

Velocity-Distance Relation among Extra-Galactic Nebulae.

Figure 2.1: Hubble expansion plot. This is Edwin Hubble's plot of the velocity - distance relation of 20 galaxies. The vertical axis plots cz and the units should be in km/s instead of km. (from Hubble 1929, Proc. Nat. Acad. Sci., 15, 168)

It should be noticed that $z = v/c$ is the non relativistic relation for the Doppler shift, but Hubble was able to use that since all the galaxies he studied had very low redshift (Ryden, 2016).
However, Hubble flow was actually first discovered in 1927 by Belgian physicist and priest Georges Lemaître, who noticed that the more distant galaxies had a greater redshift (Panek, 2020). He also proposed the theory of the Big Bang, which would explain the recession of galaxies (Encyclopaedia Britannica).
Hubble just came to the same conclusion two years later, independently. Lemaître's contribution to the discovery of the Hubble-Lemaître law is less known partly because his original work was published in French is a little-known journal by the name *Annales de la Société Scientifique de Bruxelles* and partly because the derivation of the constant was omitted in the English translation of 1931 (Gibney).
Now the Hubble constant is used to determine distances to objects and the age of the universe. It is also used to "predict" the future of the universe (Panek, 2020), as from this value it is possible to know when the universe will have expanded so much that there will be nothing left in the observable universe.

2.3 Hubble Tension

Since the discovery of the expansion of the universe the value of the Hubble constant has been reason for discussion between astronomers.
Hubble himself thought that the constant should have been 500 km/s/Mpc. This value was calculated by determining the period-luminosity relation of Cepheids to calibrate the distance to M31 and using that to calculate the distance to farther away galaxies.
Such a high value would have meant an Hubble time of only 2 Gyr old, however the Earth itself had been dated from radioactive rocks to be at least 3 Gyr old (Huchra), meaning that his estimate had to be wrong. In fact, Hubble had underestimated the distance to the galaxies, due to a wrong calibration of the period-luminosity relation of Cepheids.
In the 1950's, about 20 years after Hubble's estimate of the constant, the period-luminosity relation of Cepheids was re-calibrated, which solved the problem of the Earth being older than the universe (Huchra). This re-calibration was achieved by Walter Baade, who discovered the existence of 2 types of Cepheids (Huchra).
However in the 1970's, controversy sparked again when two groups, one lead by Allan Sandage and one lead by de Vaucouleurs, obtained, respectively, values of 50 km/s/Mpc and 100 km/s/Mpc (Huchra).
In 2001 this discrepancy was solved when the Hubble Space Telescope Key Project produced its first measurement of the Hubble constant which settled the constant at 72 ± 8 km/s/Mpc, right in the middle of the disputed values (Freedman et al., 2001). This measurement was achieved through the use of Cepheids to calibrate secondary distance indicators, far enough to be subject to Hubble flow (Freedman et al., 2001).
Another search for the value of the Hubble constant was carried out by the SH0ES project, using both Cepheids and Supernova Ia to calibrate distances. The most recent result, produced in 2019 is 74.03 ± 1.42 km/s/Mpc (Riess et al., 2019), which is in perfect accordance with the first Key Project value. Both these methods involve calibrating distances of far away objects starting from closer objects, and climbing the steps of the cosmic ladder.
Another method that has been used to calculate the Hubble constant is the analysis of the size the cosmic microwave background temperature fluctuations (NASA, b). This method was used by the Wilkinson Microwave Anisotropy Probe (WMAP) and by the *Planck* mission. The most recent *Planck* data points to an $H_0 = 67.4 \pm 1.4$ km/s/Mpc (Planck Collaboration et al., 2018). Clearly, the two measures, one found using the CMB and one found using the Cosmic Distance Ladder, do not agree. Even more worrisome, is that their difference is around 3σ, a very statistically significant difference (NOVA). Such a difference might mean that some unknown physics is at play.
Another standard candle that has been used to calculate the Hubble constant is red giants (NASA, a). The value of H_0 that was found using this method is 69.8 ± 0.8 km/s/Mpc (Freedman et al., 2019), almost right in the middle of the other values found with Cepheids and the CMB.

The difference in inferred constant over time, from these three methods, can be seen in figure 2.2. It can be seen that at the beginning of the century the measurements were overlapping but now they are getting further and further away from each other.
In figure 2.3, an overview of recent H_0 estimated, with their errors is represented. These estimates are divided in late and early Universe.
The difference between late and early Universe measurement is, to put it simply, that early Universe data probes the early Universe, so the CMB, without using nearby objects as calibration, instead the late Universe data infer the Hubble constant from the nearby Universe.
Such different values, as can be seen in figure 2.3, might be due by measurement errors, maybe a broken step in the cosmic ladder. However the CMB measurements have now reached an uncertainty of only 0.5%, the cosmic ladder measurements from Cepheids have reached an uncertainty of only 2.4 %, but the measurements are still not even close to converging (Reiss, 2016).
It is also very interesting to notice from figure 2.3 that the early Universe measurements perfectly agree with each other and the late Universe measurements seem to mostly agree with each other, which is something that begs for explanation and might imply that the difference is not just mere calibration error.
Another factor, other than measurement error, that could lead to this discrepancy is a misunderstanding of how the universe grows (Panek, 2020). This misunderstanding might be due to an uncertainty about how may particles there are in the Universe, maybe there exists another kind of neutrino that has not been taken into account in models on the growth of the Universe because it has never been observed so its existence is unknown. Such a neutrino would change the energy and mass distribution, leading to the expansion working in a different way (Panek, 2020). Another possible explanation is dark energy. No one yet knows what is it nor how it works, and a change of its effect in time might be the cause of this discrepancy (Panek, 2020).
Another possible explanation is that the Milky Way might be at the center of a local void (NOVA). In that case, the velocity at which objects appear to move away would be higher than just the Hubble flow, since matter would also be drawn to higher density regions (NOVA). This theory is what will be analyzed in this thesis.
This will be done initially by constructing a simple model with multiple voids present. The matter inside the voids will be given a velocity pointing radially outward. Lines of sight will then be taken both from inside and outside voids and the values of the inferred Hubble constant in these two cases will be compared to theory values.
Subsequently, an N-body ΛCDM simulation will be analyzed. The Nexus formalism will be used to identify structure and then lines of sight will be taken from voids, filaments, nodes and walls. Those values will once again be compared to theory values.
Both the N-body ΛCDM simulation and the Nexus formalism will be explained later.

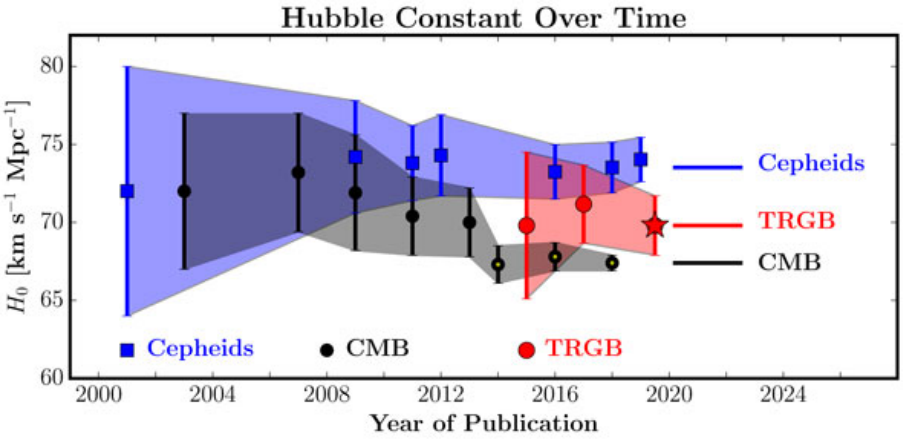

Figure 2.2: Values of H_0 over the years. Here are represented values of H_0 with the associated error from three different methods during the years. It can be seen that they were overlapping but now appear to diverge from each other. (from Freedman et al. / Astrophysical Journal)

Then, from the ΛCDM simulation, the dark matter halos will be identified and lines of sight will once again be taken from the different kinds of structure, analyzing the radial velocity - distance relation of these halos.

2.3.1 Methods for measuring H_0

In figure 2.3 multiple methods are present, most of which have already been mentioned in the previous section. To have a better understanding of the problem of Hubble tension, is good to understand how the different methods work.

2.3.2 Early Universe measurements

In the top third of figure 2.3 two early Universe measurements are present. These measurements use physics at the other end of cosmic history to reach their H_0 values and in the meantime also provide a good check on ΛCMD cosmology (Abitbol et al., 2020). The determination of the Hubble constant from the Cosmic Microwave Background uses the standard-ruler sound horizon measured by CMB anisotropy observations (Abitbol et al., 2020). This method can also be employed without using CMB data but by using baryon acoustic oscillation, Big Bang nucleosynthesis, and weak lensing data (Abitbol et al., 2020), all of which are used to reach the value in light grey in figure 2.3.
The value of the Hubble constant can be found from the evolution of the temperature of the CMB monopole, since T_{CMB} and $a(t)$ can be mapped onto

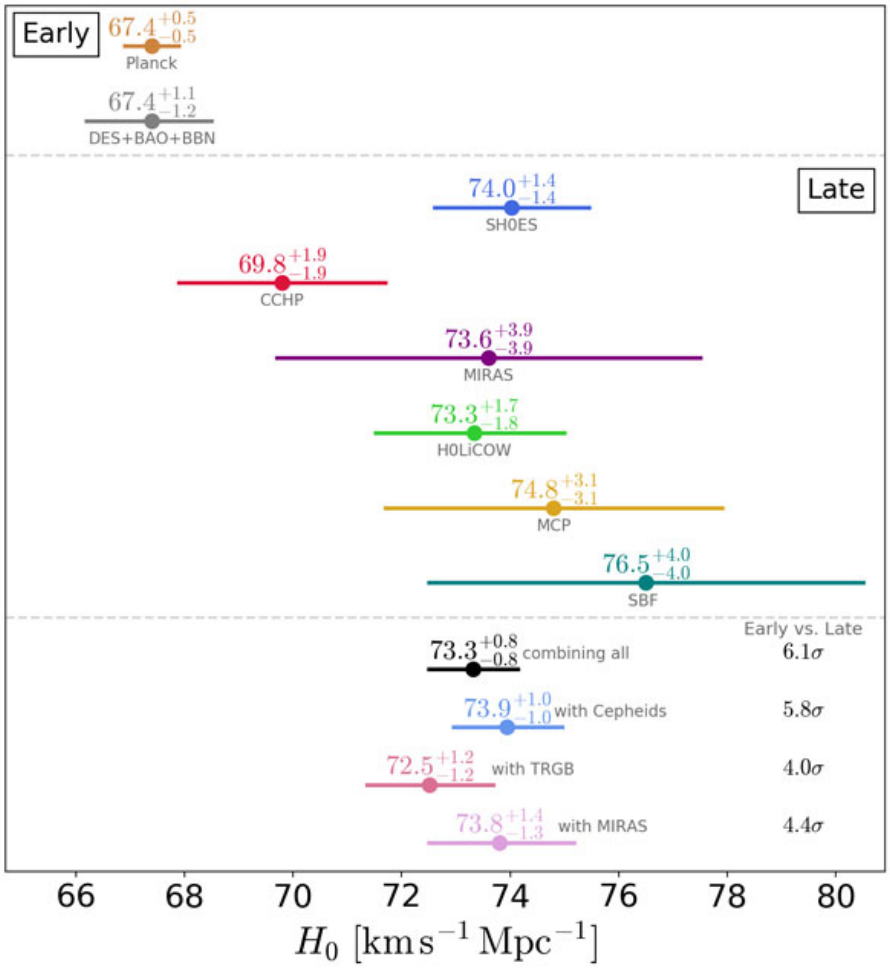

Figure 2.3: H_0 calculated with various methods. Here is a representation of the values of H_0 with the associated errors obtained from different research groups, both in the early and late universe. In the bottom are the average values each method. (from Vivien Bonvin / HOLiCOW Team)

each other (Abitbol et al., 2020), and, as already mentioned, $H_0 = (\dot{a}/a)_{t=t_0}$.

2.3.3 Late Universe measurements

In the middle third of figure 2.3, the measurements for the late Universe are present.

Cepheids and SNe Ia as standard candles

The first measurement, in blue, was performed by the SH0ES team. The SH0ES team has spent the past 15 years building a distance ladder using geometric distances to calibrate Cepheids, followed by 19 hosts to both SNe Ia and Cepheids, followed by hundreds of type Ia Supernovae in the Hubble flow (Verde et al., 2019). Once the ladder has been built, finding the Hubble constant is not difficult, as both velocities and distances are known.
Cepheids and type Ia Supernovae are the basis of this ladder since they are very reliable standard candles. Cepheids are pulsating stars and the period of their pulsation is related to their luminosity in a very predictable way, making the luminosity very easy to calculate. Type Ia supernovae, instead, have a very predictable luminosity peak, making the apparent magnitude dependent on distance in a predictable way.

Tip of the Red Giant Branch

Another method that has been used to determine the Hubble constant is the tip of the red giant branch method, TRGB, which has been used by the CCHP team. Their measurements can be seen both in figures 2.3 and 2.2. This method also calibrates distances to farther away objects using standard candles, but it is based on red giants and Supernovae Ia, instead of Cepheids. When red giants are on the verge of extinction they undergo a helium flash, which indicates their luminosity reliably and can thus be used as a standard candle (Freedman et al., 2019).

Gravitationally lensed quasars

Both these methods have to go through standard candles, but there are also some that are independent of them. One of these methods is being used by the HOLiCOW team, whose value is represented in green in figure 2.3, and it involves looking at gravitationally lensed quasars. When an object, the source, is gravitationally lensed into multiple images, the light rays will take different paths through space-time to the images. Since these paths have different lengths, light rays will arrive to the images at different times. If the source is variable, this time difference can be easily measured (Wong et al., 2020). The time delay is related to a quantity called "time delay distance" which is itself primarily sensitive to H_0 (Wong et al., 2020). This measurement is therefore completely independent of the cosmic distance ladder and

since the distances probed with this method are very large the measurement is not influenced by the velocity field of the local Universe (Wong et al., 2020).

Chapter 3

Voids

Matter in the Universe, in the hundreds of Megaparsecs scale, is distributed in a web-like pattern, called the cosmic web. This pattern represents the largest non-linear structure in the Universe (Cautun et al., 2014).
Voids are a prominent aspect of the cosmic web, with sizes in the 20-50 Mpc h^{-1} range, even though an upper limit has not been set yet (van de Weygaert, 2014). They are particularly devoid of galaxies, have a usually almost spherical shape and they occupy most of the space in the universe, even though they are estimated to contain only about 15 % of the total mass (van de Weygaert, 2014), as can be seen in figure 3.1. They are surrounded by walls, filaments, and nodes, which are other prominent features of the cosmic web.
Voids are very interesting for many reasons. First of all, their prominence in the cosmic web makes it so that understanding voids is a necessary step to understand the formation and dynamics of the cosmic web (van de Weygaert and Bond, 2008). Voids may also contain important information about the cosmological parameters (van de Weygaert and Bond, 2008) as it has been realized that their structure, morphology, and dynamics reflects the nature of dark energy, dark matter and that of the possibly non-Gaussian nature of the primordial perturbation field (van de Weygaert, 2014). Lastly, voids are very interesting subjects because, thanks to the low density, they are a great candidate to study the effects of the cosmic environment on the formation of galaxies (van de Weygaert and Bond, 2008).
In a void based description of the universe, voids represent the transition scale at which density perturbations have decoupled from the Hubble flow (van de Weygaert, 2014).
Voids originate from troughs in the primordial Gaussian density field (van de Weygaert and Bond, 2008) so their density is lower than that of the background universe. Because of this, their internal gravity is weaker and matter will thus stream out of the void while it is expanding with respect to the Universe, in a superHubble motion (van de Weygaert and Bond, 2008). As a consequence of this, voids become more and more empty as time goes by. An isolated, ideal void would asymptotically evolve to $\delta = -1$, which is complete

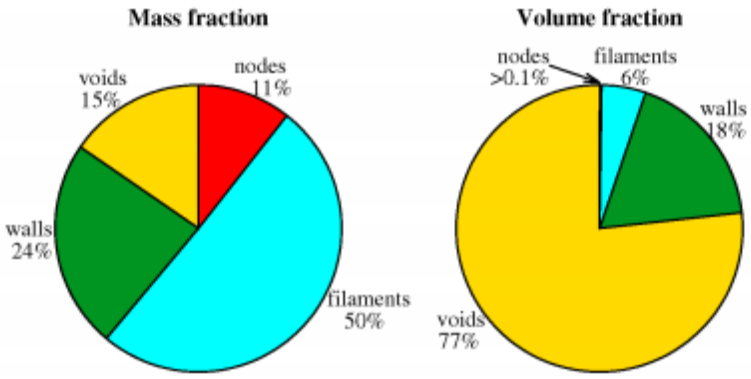

Figure 3.1: Mass and volume fraction occupied by each cosmic web environment (from van de Weygaert (2014))

emptiness (van de Weygaert and Bond, 2008). Here, δ represents the density perturbation profile and it is defined as (Sheth and van de Weygaert, 2003)

$$\delta(r,t) = \frac{\rho(r,t)}{\rho_u(t)} - 1 \tag{3.1}$$

where $\rho(r,t)$ is the density of the void and $\rho_u(t)$ is the density of the universe. Voids never actually reach $\delta = -1$ since they are not isolated entities but embedded in a cosmic web of walls, filaments, nodes, and more voids.
As already mentioned, voids expand in a superHubble motion, which means that their expansion is faster than the Hubble flow, so they are not only expanding as a consequence of the Universe expanding, but they are expanding with respect to the Universe itself (van de Weygaert and Bond, 2008). As a result of this expansion, voids are the key to understand matter distribution in the Universe (van de Weygaert, 2014)(van de Weygaert and Bond, 2008). When voids expand, matter is squeezed between them, forming filaments and walls on void boundaries (van de Weygaert and Bond, 2008). Understanding void expansion is thus fundamental to understand how the cosmic web formed.
This view was endorsed and expanded by the SDSS and 2dFGRS surveys (van de Weygaert, 2014), thanks to maps like that seen in figure 3.2. Such a map makes the central role of voids in the distribution of matter in the Universe, evident. Some studies have also noted the prominence of voids in the early and distant Universe (van de Weygaert, 2014).
It was also already mentioned that voids are usually round in shape. This is because gravitational acceleration is stronger on shorter axes so any aspherical underdensity will become more spherical as it expands (van de Weygaert and Bond, 2008). In reality, a void will never be a perfect sphere because of environmental factors (van de Weygaert and Bond, 2008). This is also visible in images of simulations, like in figure 3.3. There, an evolving void can be seen.

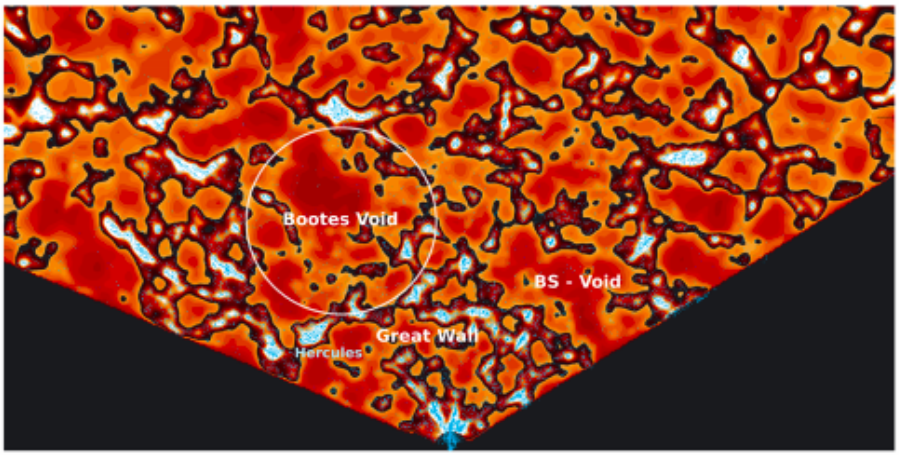

Figure 3.2: SDSS density map and galaxies in a region of the SDSS galaxy redshift survey region containing the canonical Bootes void. The underdense voids are clearly outlined as the lighter region outside the high-density weblike filamentary and wall-like features. (from van de Weygaert (2014))

Its expansion is evident and it can be seen that it becomes more round as it expands, even though it never actually reaches the shape of a perfect sphere. For this project, the velocity field of voids will be their most important feature, since this velocity is what would affect the measurements of the Hubble constant in the local Universe, in case the Milky Way was at the center of a void. Fortunately, the velocity field of uniform density voids is quite easy to understand (Sheth and van de Weygaert, 2003). An observer in a void would observe a Hubble type velocity, with objects farther away moving away faster than objects close to the observer (Sheth and van de Weygaert, 2003). Essentially, an isolated void can be treated as its own Friedmann universe, meaning that the equations of motion of the void assume the same form as the Friedmann-Robertson-Walker-Lemaître equations, with a different Ω value (Sheth and van de Weygaert, 2003). In figure 3.4 a real life example of the velocity field of a void can be seen. The arrows indicate the field and it can clearly be seen in the zoomed-in part on the right, that they are pointing outward from the center void, indicating an outward motion of matter from the void.

3.1 Spherical Model

The spherical model is a simple model used to understand the evolution and the main characteristics of isolated over/underdense regions (Sheth and van de Weygaert, 2003). For the purpose of this thesis, this model will only be used to analyze the characteristics of an isolated void, thus subjects strictly related

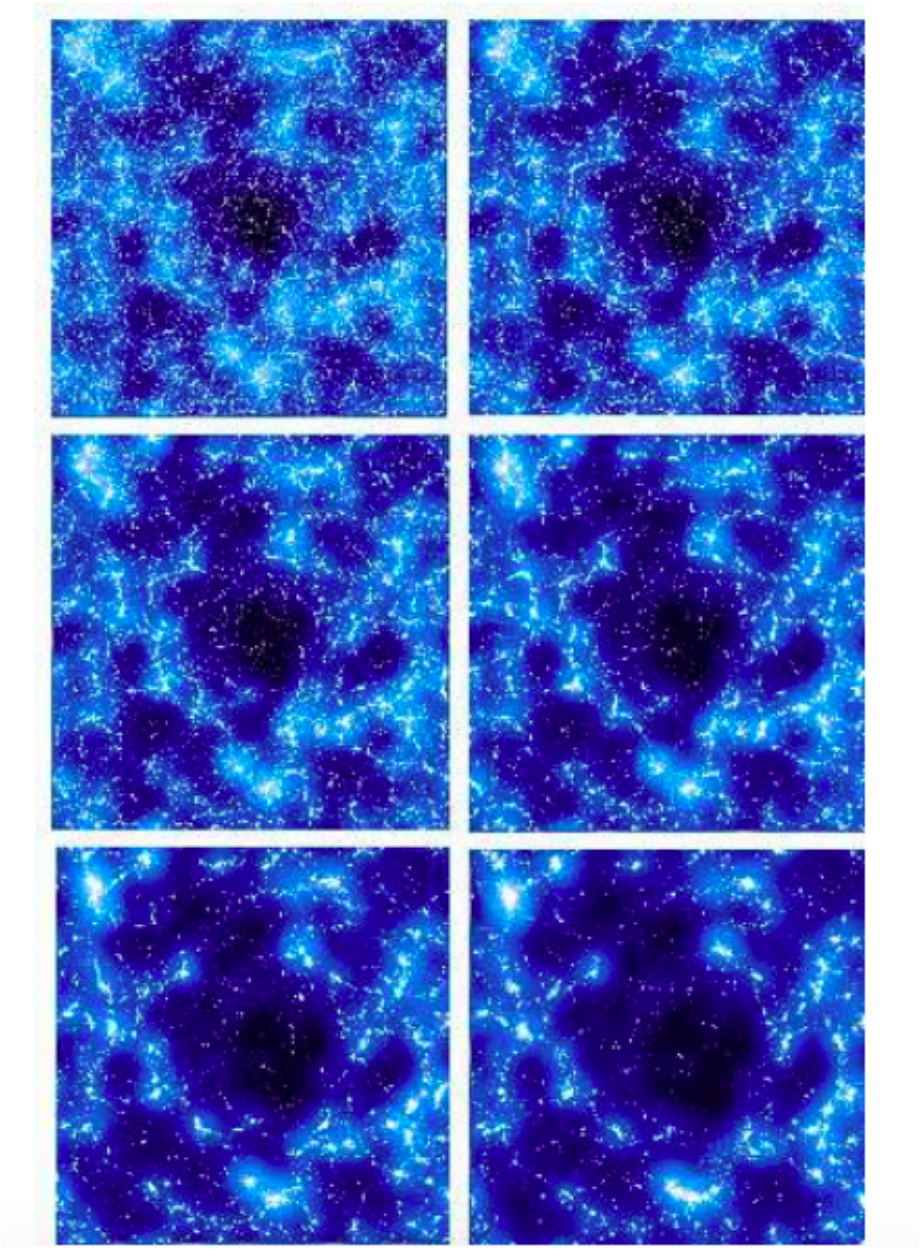

Figure 3.3: Simulation of an evolving void in a ΛCDM scenario. (from van de Weygaert and Platen (2011))

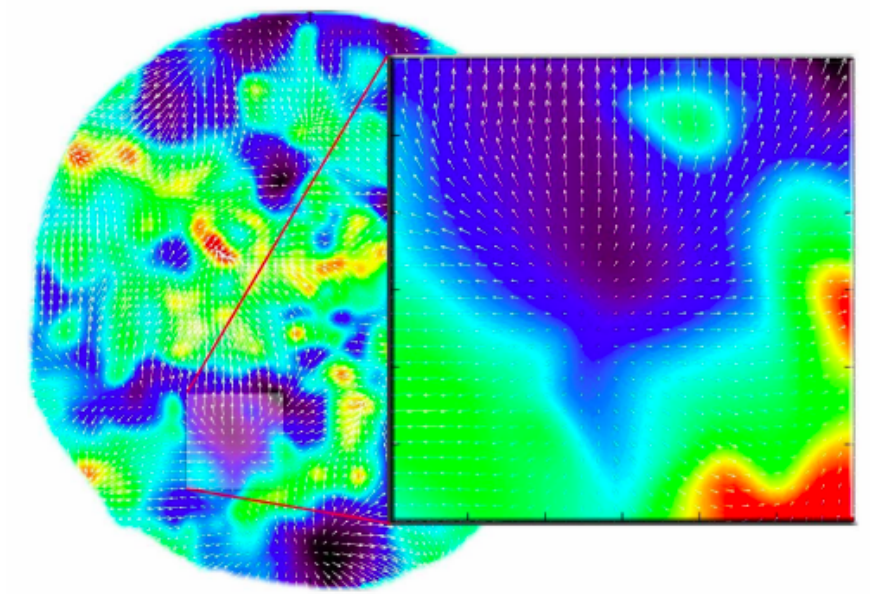

Figure 3.4: Gravitational impact of the Sculptor Void. The righthand frame shows the inferred velocity field in and around the Sculptor void near the Local Supercluster. The color map represents the density values, with dark blue at $\delta \approx$ - 0.75 and cyan near $\delta \approx 0.0$. The vectors show the implied velocity flow around the void, with a distinct nearly spherically symmetric outflow. It is a zoom-in onto the indicated region in the density and velocity map in the Local Universe (lefthand) determined based on the PSCz galaxy redshift survey. From: Romano-Diaz & van de Weygaert 2007

to overdensities will not be mentioned.
The spherical model starts by assuming the void to be spherical, as the name might suggest, which, as already mentioned, is a very good approximation, and it treats the void in terms of mass shells, so as concentric shells (Sheth and van de Weygaert, 2003). It is also assumed that there is no substructure in the void so all the shells are perfectly uniform (Sheth and van de Weygaert, 2003). The evolution of the shells thus solely depends on the total mass contained within the shell and on the background cosmological density (Sheth and van de Weygaert, 2003).
During this thesis, the background universe is assumed to be an Einstein-de Sitter universe, a matter dominated universe with zero curvature (Watson, 2000). The initial density profile of the void is assumed to be a bucket distribution, meaning that the underdensity is constant through the whole void, until a sharp jump at the edges. This assumption makes the model simple but still useful.
The model which will be explained in this chapter is a spherical representation of what will be seen later in the simulation. Here it will be shown that voids are emptying, as can be seen from figure 3.5, and the deeper they are the faster matter flows out.

3.1.1 Definitions

Shells start from a physical radius r_i at time t_i and their initial motion is formulated by (Sheth and van de Weygaert, 2003):

$$r_i = r(t_i) = a(t_i)x(t_i) \tag{3.2}$$

where $x(t_i)$ is the initial comoving radius and $a(t_i)$ is the initial scale factor of the shell. The expansion of the shells in terms of time is characterized by the expansion factor $R(t, r_i)$ as:

$$r(t, r_i) = R(t, r_i)r_i \tag{3.3}$$

where $r(t, r_i)$ is the physical radius of the shell with initial radius r_i at time t (Sheth and van de Weygaert, 2003). The evolution of the shell is dictated by the cosmological density parameter

$$\Omega(t) = \frac{8\pi G\rho_u(t)}{3H_u^2} \tag{3.4}$$

and by the mean density contrast within the radius of the shell

$$\Delta(r, t) = \frac{3}{r^3}\int_0^r \delta(y, t)y^2 dy \tag{3.5}$$

with δ defined in equation 3.1. $\Delta(r, t)$ is a relative quantity, as it compares the density of a mass shell to the density of the background universe.

The evolution of the expansion factor $R(t, r_i)$ can be determined by solving the equations of motion of a shell at radius r, which are (Sheth and van de Weygaert, 2003):

$$\frac{d^2r}{dt^2} = -\frac{GM}{r^2} \tag{3.6}$$

$$\frac{1}{2}\left(\frac{dr}{dt}\right)^2 - \frac{GM}{r} = E \tag{3.7}$$

In these equations E indicates the energy of the shell which is constant, and M is the mass contained within the shell of radius r, which is also constant if we assume that there is no shell crossing (Sheth and van de Weygaert, 2003). To determine the evolution of $R(t, r_i)$ it is useful to define the parameters $\Delta_{ci} = \Delta_c(t_i)$ and α_i which are defined as (Sheth and van de Weygaert, 2003):

$$1 + \Delta_{ci} = \Omega_i(1 + \Delta(r_i, t_i)) \tag{3.8}$$

$$\alpha_i = \left(\frac{v_i}{H_i r_i}\right)^2 - 1 \tag{3.9}$$

where $\Omega_i = \Omega(t_i)$ and v_i is the physical velocity, which means the sum of Hubble expansion and peculiar velocity, at time t_i.
At time t_i the peculiar velocity of a spherical perturbation is (Sheth and van de Weygaert, 2003):

$$v_{pec,i} = -\frac{H_i r_i}{3} f(\Omega_i)\Delta(r_i, t_i) \tag{3.10}$$

which leads to:

$$\alpha_i = -\frac{2}{3} f(\Omega_i)\Delta(r_i, t_i) \tag{3.11}$$

The parameters just defined can be further explained as Δ_{ci} being the density contrast with the critical universe and α_i being the peculiar velocity of the shell (Sheth and van de Weygaert, 2003). Since in this thesis it is assumed that the void is embedded in an EdS universe then the critical density contrast will be the same as the density contrast ($\Delta_c(r, t) = \Delta(r, t)$).
The evolution of a shell is solely determined by the underdensity inside the radius r_i, and by the velocity perturbation (Sheth and van de Weygaert, 2003). This means that the evolution solely depends on Δ_{ci} and α_i. From this, three cases can be distinguished:

- Open shell: $\alpha_i > \Delta_{ci}$
- Critical shell: $\alpha_i = \Delta_{ci}$
- Closed shell: $\alpha_i < \Delta_{ci}$

3.1.2 Shell Solutions

The two cases relevant for this thesis are the open system and the critical system. Inside the void, the shells are constantly expanding, whereas, outside of the void the shells are still. For an open system the solutions to the equations of motions will be (Sheth and van de Weygaert, 2003):

$$r(\Phi) = \frac{GM}{2E}(\cosh(\Phi) - 1) \tag{3.12}$$

$$t(\Phi) - t_i = \frac{GM}{2E\sqrt{2E}}(\sinh(\Phi) - \Phi) \tag{3.13}$$

Where Φ is the development angle, which parametrizes all physical quantities relating to the mass shell (Sheth and van de Weygaert, 2003).
For a critical system, the solution to the equations of motion will be (Sheth and van de Weygaert, 2003):

$$r(t) = (\frac{9}{2}GM)^{1/3}(t - t_i)^{2/3} \tag{3.14}$$

It can be noticed that for a critical shell the dependency of r on t can be found directly, so there is no need to involve the development angle.
The definitions for Δ_{ci} and α_i that were given in the previous section can be adapted to include time dependence by changing t_i to t and those can be used to find expressions for E and GM, which will be (Sheth and van de Weygaert, 2003):

$$E = \frac{1}{2}H_i^2 r_i^2 \,(\alpha_i - \Delta_{ci}) \tag{3.15}$$

$$GM = \frac{1}{2}H_i^2 r_i^2 (1 + \Delta_{ci}) \tag{3.16}$$

Combining equations 3.15 and 3.16 with equations 3.12 and 3.13 the solutions for the equations of motion for an open shell in terms of Δ_{ci} and α_i can be determined. They will be (Sheth and van de Weygaert, 2003):

$$R(t, r_i) = \frac{1}{2}\frac{1 + \Delta_{ci}}{\alpha_i - \Delta_{ci}}\,(\cosh(\Phi) - 1) \tag{3.17}$$

$$H_i(t - t_i) = \frac{1}{2}\frac{1 + \Delta_{ci}}{(\alpha_i - \Delta_{ci})^{3/2}}\,(\sinh(\Phi) - \Phi) \tag{3.18}$$

The same can be done for a critical shell, this time using equations 3.15, 3.16 and 3.14 (Sheth and van de Weygaert, 2003).

$$R(t, r_i) = \left(\frac{3}{2}H_i(1 + \Delta_{ci})^{1/2}(t - t_i)\right)^{2/3} \tag{3.19}$$

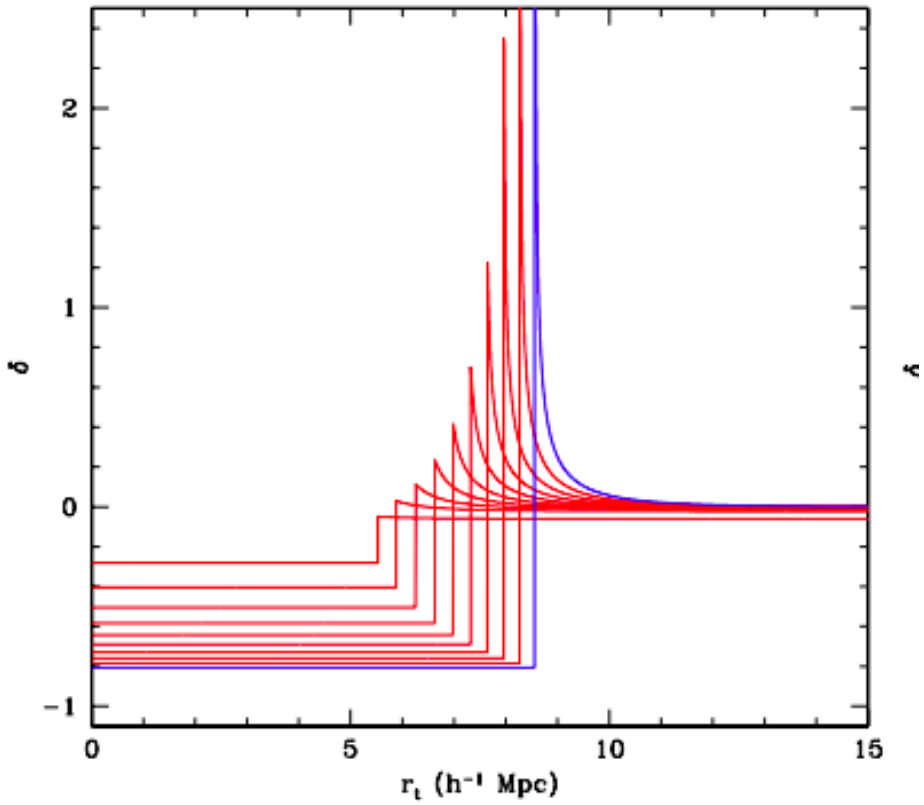

Figure 3.5: Time evolution of the density contrast of a tophat void. Here the density contrast evolution of a tophat void until the epoch of shell crossing can be seen. Each line represents a time step. It can be seen that the density contrast reaches -0.8 at shell crossing. (from van de Weygaert and Platen (2011))

3.1.3 Density Evolution

To understand how a shell evolves it is important to understand its density contrast evolution in time, which is (Sheth and van de Weygaert, 2003):

$$1 + \Delta(r,t) = \frac{1 + \Delta_i(r_i)}{R^3} \frac{a(t)^3}{a_i^3} \tag{3.20}$$

In the case of an Einstein-de Sitter universe, the density contrast can be written in an easier way as:

$$1 + \Delta(r,t) = \frac{9}{2} f(\Phi) \tag{3.21}$$

Where $f(\Phi)$ is the cosmic density function:

$$f(\Phi) = \begin{cases} \frac{(\sinh(\Phi)-\Phi)^2}{(\cosh(\Phi)-1)^3} & \text{Open} \\ \frac{2}{9} & \text{Critical} \\ \frac{(\Phi-\sin(\Phi))^2}{(1-\cos(\Phi))^3} & \text{Closed} \end{cases} \tag{3.22}$$

It is important to notice that the function $f(\Phi)$ is valid both for shells (where open means $\alpha_i > \Delta_{ci}$) and for the background universe (where open means $\Omega < 1$) (Sheth and van de Weygaert, 2003).

3.1.4 Shell Velocities

For the purpose of this thesis, the velocity field of matter in voids is of great interest.
The velocity of a shell is defined as (Sheth and van de Weygaert, 2003):

$$v(r,t) = \frac{dR}{dt} r_i \tag{3.23}$$

What is actually more interesting is the peculiar velocity, which is the total velocity minus the Hubble motion, so $v_{pec}(r,t) = v(r,t) - H(t)r(t)$. From this is possible rewrite the peculiar velocity as (Sheth and van de Weygaert, 2003):

$$v_{pec}(r,t) = \frac{3}{2} H(t) r(t) \left(g(\Phi) - \frac{2}{3} \right) \tag{3.24}$$

where $g(\Phi)$ is (Sheth and van de Weygaert, 2003):

$$g(\Phi) = \begin{cases} \frac{\sinh(\Phi)(\sinh(\Phi)-\Phi)}{(\cosh(\Phi)-1)^2} & \text{Open} \\ \frac{2}{3} & \text{Critical} \\ \frac{\sin(\Phi)(\Phi-\sin(\Phi))}{(1-\cos(\Phi))^2} & \text{Closed} \end{cases} \tag{3.25}$$

In figure 3.6, the velocity evolution of a model void can be seen. Each line represents a step in time, with the solid line being the velocity field in the present. It can be seen that at the present time the velocity is faster at the edges of the void, indicating an outflow of matter.

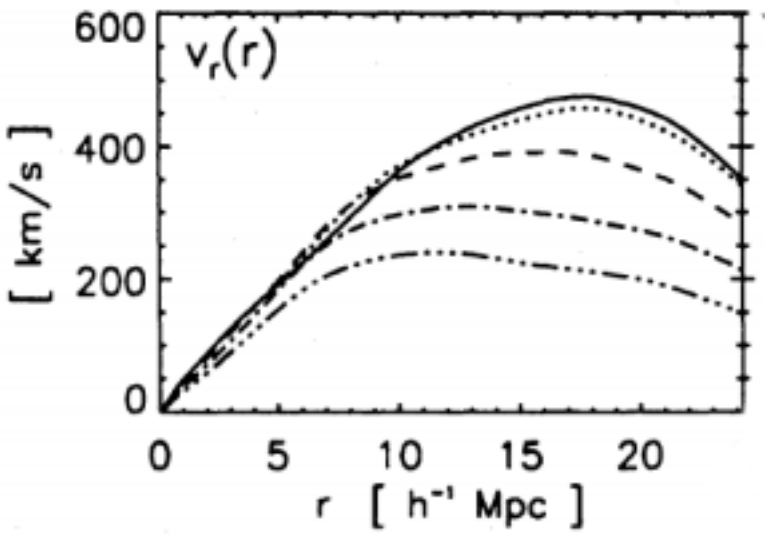

Figure 3.6: superHubble expansion. Velocity profiles of an evolving void in a constrained simulation of a void in a CDM cosmology. Each line represents a different time at which the profile is found. (from van de Weygaert (2014))

3.1.5 Shell Crossing

The peculiar acceleration directed outward is directly proportional to $\Delta(r, t)$. In the generic case, the inner shells feel a stronger density deficit and thus a stronger outward acceleration, than outer shells (Sheth and van de Weygaert, 2003).
As a consequence of the differential expansion within and around the void, and the decrease of the expansion rate with radius r, shells start to accumulate matter toward the edge of the void (Sheth and van de Weygaert, 2003). The density deficit thus decreases as a function of the radius, with a minimum at the center of the void (Sheth and van de Weygaert, 2003). Since the peculiar velocity of a shell scales with the density deficit, shells that were originally in the inner parts of the void start catching up to shells in the outer parts of the void and eventually pass them. This event is called *shell crossing* (Sheth and van de Weygaert, 2003). The corresponding increase in density will turn the edge of the void into an infinitely dense ridge and from this moment on, the evolution of the void can be described by a self-similar, outward moving shell (Sheth and van de Weygaert, 2003). This evolution can be seen in figure 3.5, where multiple time steps are present, from the starting tophat void ending in a very underdense void in the center with a very dense ridge at the edge.
For a top-hat void in an Einstein-de Sitter universe the shells initially just

outside of the void's edge go through shell crossing at a well determined development angle value (Sheth and van de Weygaert, 2003). This value can be found from:

$$\frac{\sinh\Phi_{\rm sc}(\sinh\Phi_{\rm sc}-\Phi_{\rm sc})}{(\cosh\Phi_{\rm sc}-1)^2}=\frac{8}{9}\ ,\ \text{so}\ \Phi_{\rm sc}\approx 3.53 \tag{3.26}$$

At this development angle, the average density in the void is given by

$$1+\Delta(r,t)=0.1982 \tag{3.27}$$

This means that the shell has expanded by a factor $(0.1982)^{-1/3}\ \approx\ 1.7151$ (Sheth and van de Weygaert, 2003).
For a spherical void, shell crossing marks a dynamical phase transition. The time of shell crossing is entirely determined by the global density parameter Ω_i, the initial density deficit of the shell Δ_i and by the steepness of the density profile (Sheth and van de Weygaert, 2003). From this link it is possible to predict the non linear evolution of cosmic voids.

3.2 Voids and the Hubble constant

It was already mentioned that one of the theories on why the Hubble constant measurements are not uniform involves voids. Some say that if the Milky Way was at the center of a local void, it could explain why the late and early Universe measurements of the Hubble constant are not agreeing, and it could also explain why the early Universe measurements are always lower values than the late Universe ones.
If the Milky Way was at the center of a local void it would cause the surroundings to move away faster than expected, due to matter being drawn to higher density regions (NOVA). This would cause a wrong measurement of the Hubble constant, which would be fixed by subtracting this extra velocity to the measurements. This fix should bring the value closer to the CMB value (NOVA).
Some think that this explanation is flawed because there is not a drop-off in measured H_0 at any redshift, which could indicate the existence of such a void (Kenworthy et al., 2019). The only changes in the local density that have been identified are deemed not substantial enough to explain the discrepancy between the early and late Universe measurements (Kenworthy et al., 2019).
Others think that even if the Milky Way was in the center of a void, the kind of tension between the values seen now could only be explained by a void so big its existence would be very unlikely (Wu and Huterer, 2017).

Chapter 4

Bubble Model

Here a model based on spherical voids will be described. This model will be used to get a first insight into how clustered voids might influence the outcome of the measured recession velocity. In this chapter, a short explanation of how the model was built and how the radial velocity - distance relation was probed can be found. The results of this analysis will be presented in the next chapter.

4.1 Building the model

Before moving to the ΛCMD N-body simulation, a bubble model was constructed to investigate the radial velocity - distance relation in a simpler setting. This model was initialized with 100000 particles in a box of side 100 Mpc. 100 spherical voids were then added to the simulation in different clustering distributions, as will be later explained.

4.1.1 Void clustering

To have a more realistic simulation, the voids were clustered instead of just randomly scattered across the box. This was achieved by using an adapted version of the Neymann-Scott process (Weygaert, 1994) to cluster the centers of the voids. This process requires to uniformly distribute an N_0 number of parent points and around each one of them uniformly distribute N_1 points inside a sphere of radius λ, expressed in terms of n_0, where n_0 is the number density of parent points (Weygaert, 1994). A realization of the Neymann-Scott process will contain all the offspring points (Yau and Loh, 2012), which in this case will become the centers of the voids. For this model, multiple clustering distributions have been used, as can be seen later in the thesis.

4.1.2 Creation of voids

Once this was done, each void was assigned a radius taken from a Gaussian distribution centered at 30 Mpc with a standard deviation of 5 Mpc and cut-off at 5 Mpc. This cutoff was chosen to avoid having very small voids which might not contain points. A cutoff on the biggest possible size was not used since, as already mentioned before, a maximum possible size of voids has never been found.
The number of points to be created inside such voids was determined by the density contrast to the background universe and by the number density of the background universe. The value for the density contrast of each void was taken from a Gaussian centered at -0.8, with a standard deviation of 0.1. A cutoff was placed at -1 since $\Delta = -1$ represents complete emptiness. The value for the mean of the Gaussian was chosen as -0.8 because that is the value of the density contrast of mature voids. It can safely be assumed that the voids are mature since the goal is to analyze how the Hubble constant measurements taken at this point in time might be influenced by the presence of voids. The number of points that should be present in each void was calculated from equation 3.5, and knowing that: (Sheth and van de Weygaert, 2003)

$$\delta(r,t) = \frac{\rho(r,t)}{\rho_u(t)} - 1 \tag{4.1}$$

4.1.3 Velocities

The points in the voids were also assigned a peculiar velocity of

$$v_{pec} = \frac{1}{3} H f(\Omega) \Delta r \tag{4.2}$$

whereas the points outside of the voids were assigned a peculiar velocity of $v_{pec} = 0$. This is because the points outside of the voids just move due to the expansion of the Universe, which will be added later, since the value of such velocity is based on the position of the observer. In contrast, as already mentioned, matter in voids moves in a superHubble motion, meaning that matter has a peculiar velocity due to the expansion of the void itself which is on top of the velocity due to the expansion of the universe (van de Weygaert and Bond, 2008). A 2D projection of such outward flow of matter from voids can be seen in figure 4.1. Here the velocity of matter in one isolated void is represented and it is clear that all the matter is moving outward from the center of the void. Another characteristic of the velocity of matter in voids is also clear from this figure, which is that matter farther out from the center moves away faster. One can notice that the arrows close to the center of the void are very small, almost invisible, whereas the arrows on the outside of the voids are much bigger. So from this plot, it is pretty clear that, for an observer in the center of a void, the motion of matter flowing outside of the void would resemble a Hubble expansion.

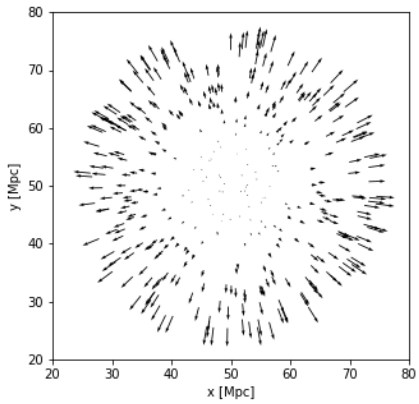

Figure 4.1: Velocity field of a single void. Matter is flowing outwards, in a superHubble motion.

For this model, H_0 was taken as 67.4 km/s/Mpc. This is important to know to understand the values that will be shown later. In the theory that is being investigated here the early Universe values are supposed to be the correct values which is the reason for this choice. That is the value reached from the *Planck* data (Planck Collaboration et al., 2018), starting from the CMB. However what is of interest is the deviation of the perceived expansion of matter from pure Hubble expansion caused by the velocities of matter in the voids and not the value of the constant itself.

4.1.4 Representations

The distribution of points and their velocity, for a clustering with 10 parent points and 10 offspring per parent can be seen in figure 4.2. In the velocity plot, it can be seen that the velocity of each point in the voids is pointing radially outward, which is what is expected, as it was just explained.
Some slices were also plotted and can be seen in figure 4.3. This was done to give a better idea of the particle distribution in space since that is difficult to clearly seen in the 3D representation of figure 4.2
In figure 4.4, some more zoomed-in slices have been plotted, to explore some features from up close.
The positions of the slices have been chosen randomly but in both figures 4.3 and 4.4 it is easy to see where there are voids present.
Not much structure other than voids can be seen since the points outside of the voids have been uniformly distributed.

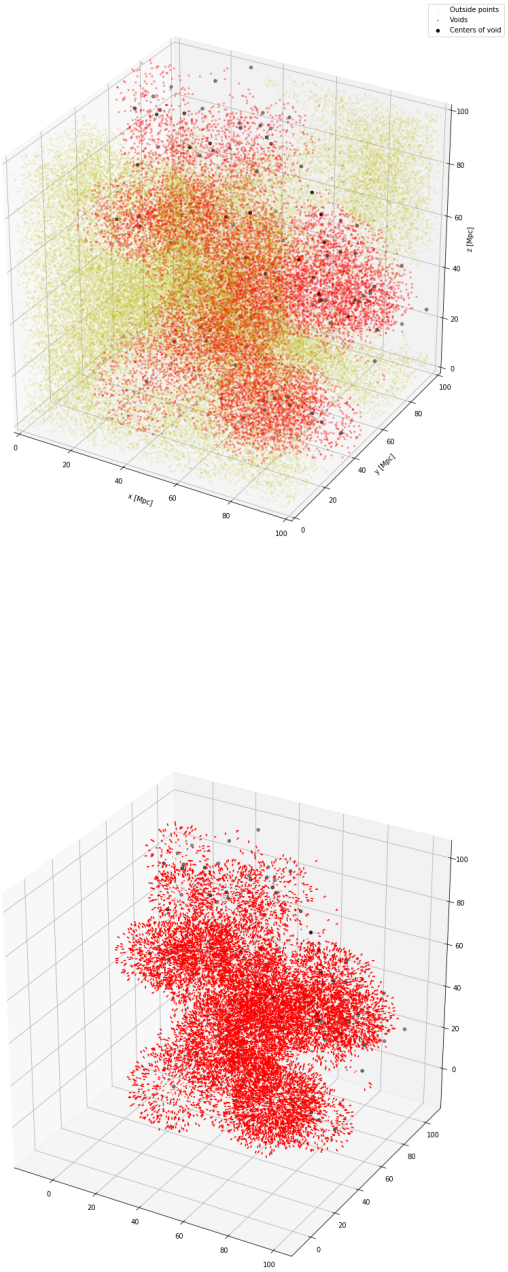

Figure 4.2: Bubble model. On top: distribution of points inside and outside the bubble voids. On the bottom: vector plot of the peculiar velocities of points inside the voids.

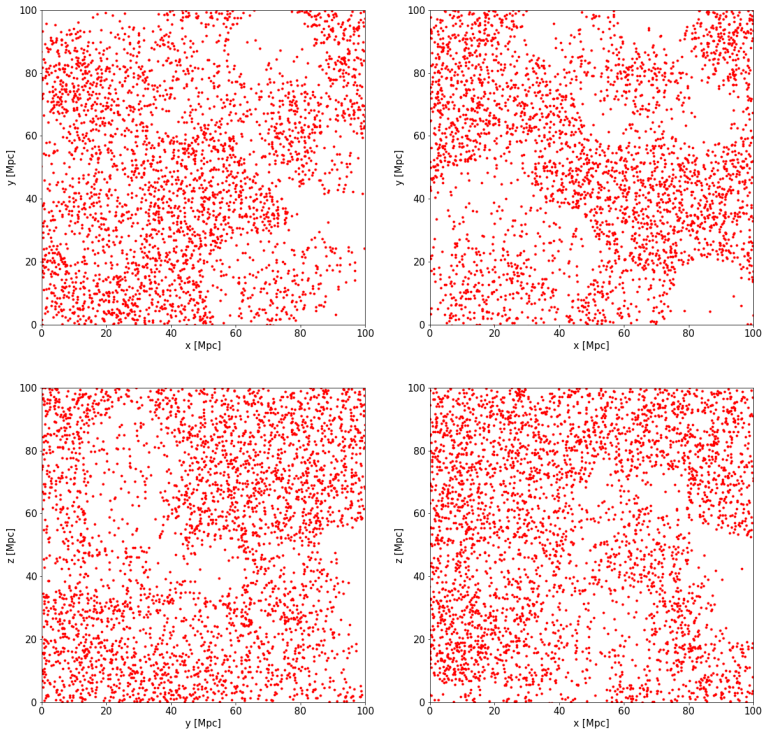

Figure 4.3: Slices through the bubble model. Here some slices taken through the simulation can be seen, to illustrate better the particle distribution. All the slices are 5 Mpc thick. The slices are taken at random places in the box. Two of them are in the z direction, so only the x and y direction are plotted, whereas the other two are one in the x and one in the y direction.

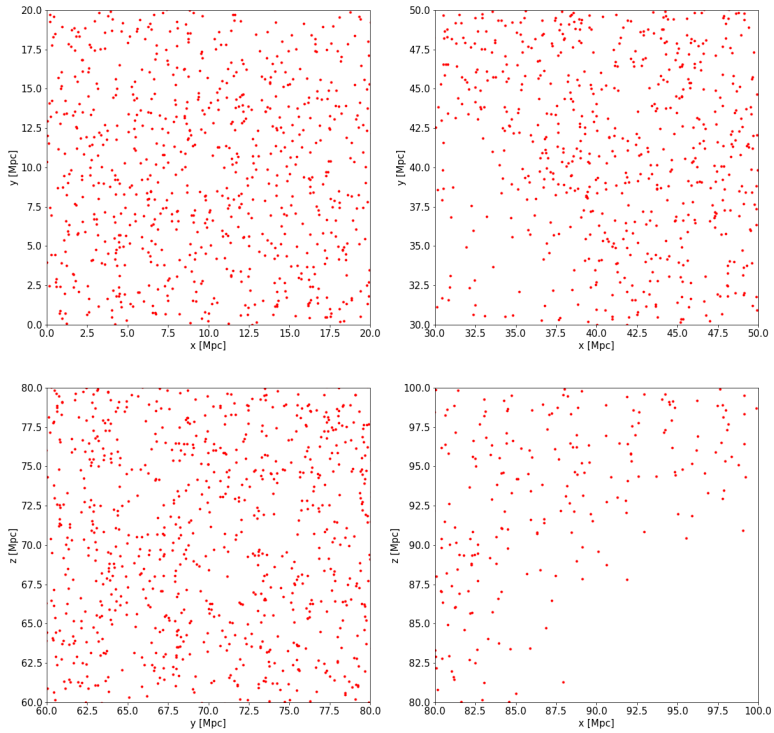

Figure 4.4: Zoomed-in slices through the bubble model. Here some zoomed-in particle distributions can be seen. These figures are a 2D representations of cubes of 20 Mpc per side, all taken in different places of the box.

4.2 Method for taking lines of sight

To achieve a good analysis of the effects voids can have on the measurement of the Hubble constants, observer positions were taken both inside and outside voids.
After the position of the observer was selected, the local Hubble constant was determined by observing the radial velocity - distance relation in multiple lines of sight around each observer.
The direction of each line of sight is specified by two angles, a polar angle and an azimuthal angle.
Once the direction was determined, usually in a random way, the points laying in a cone around that direction, with vertex at the observer position, were analyzed.
This cone shape was chosen because it is a realistic shape, as an observer looking at a solid angle of sky is effectively looking at points in a cone with vertex at the observer position. The cone was created to be quite thin, the height to radius relation for this model was chosen as 0.08. This number was picked with the aim of having enough points in the line of sight to have a sensible fit while avoiding a very wide end since, in that case, the velocities would not be anymore on the line that was chosen.
To position the cone in any given direction, with the vertex in any given position, the coordinate system was first shifted to have the new origin at the position of the observer, the vertex of the cone, and then it was rotated using the following matrix:

$$\begin{bmatrix} \cos\theta\cos\phi & -\sin\theta & \cos\theta\sin\phi \\ \sin\theta\cos\phi & \cos(\theta) & \sin\theta\sin\phi \\ -\sin\phi & 0 & \cos\phi \end{bmatrix}$$

where θ is the polar angle and ϕ is the azimuthal angle.
It should be noted that the cone wraps around the box, so no matter where the starting position is and in what direction it is oriented, a full line of sight of 100 Mpc can be found.
Since only the radial velocity of each point is needed to analyze the Hubble flow in a given line of sight, the peculiar velocity of each element was multiplied by a unit vector in the direction of the line of sight. Here again, it can be seen why a thin cone is ideal. If the end of the cone was very wide, multiplying the velocity of the point with the direction of the line of sight would not necessarily provide the radial velocity, at least in points at the outskirts of the cone. After this step, the Hubble velocity, using the value $H_0 = 67.4$ km/s/Mpc, was added to the peculiar velocity of each element, based on their distance to the observer.

Chapter 5

Results of Bubble Model

When looking at the velocities of the points in only one line of sight, something like what can be seen in figure 5.1 would be produced. In this figure, it can easily be seen where the line of sight is meeting a void as there is a dip and then a rise in the observed velocity with respect to pure Hubble expansion. This shape is due to the velocity of particles in the void being radially outward from the center. This means that when Hubble velocity is added to the peculiar velocity of those particles, from the points of view of the observer, it first looks like the matter is moving away slower than it should, and then it looks like it is moving away faster than it should. In this case, the line of sight seems to encounter only one void, hence the single dip and raise, however, the orange line in figure 5.1 could assume various shapes depending on the number of voids encountered.
A result exactly like that in figure 5.1 was expected, meaning that everything appears to works as it should.
What is interesting to analyze, though, is not just the shape of such a plot, but the best fit slope through the radial velocity - distance data points, which would give the inferred Hubble constant in that direction. The best fit was found using Linear Least Squares.
In figure 5.2 a comparison between lines of sight taken from inside and outside voids can be seen. It can easily be seen that an observer inside a void would likely find a higher value for the Hubble constant than an observer placed in the background universe. It can also be noticed that in the case of an observer inside a void the slope looks immediately steeper than in the other case. This is due to the velocity of particles closer to the observer being higher than pure Hubble expansion.
Something important to notice in figure 5.1 and figure 5.2 is that the x-axis, the distance to the observer, only goes up to 90 Mpc, whereas the box is 100 Mpc long. This was done because, when reaching those values, some artifacts are created due to the periodic boundary conditions. These artifacts could influence the fit so it was good to make the cone slightly shorter than the length on the box to avoid such influence.

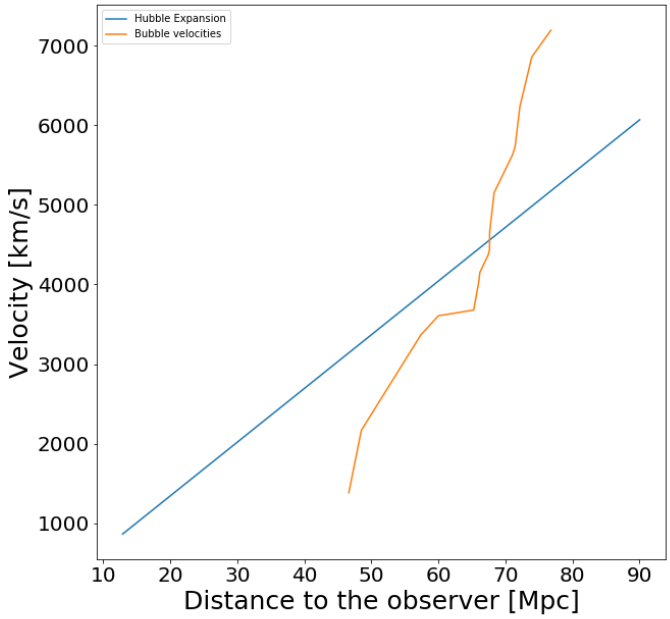

Figure 5.1: Radial velocity - distance relation in one line of sight. The blue line represents the Hubble expansion whereas the orange line represents the velocity of the particles in a void that this line of sight is meeting.

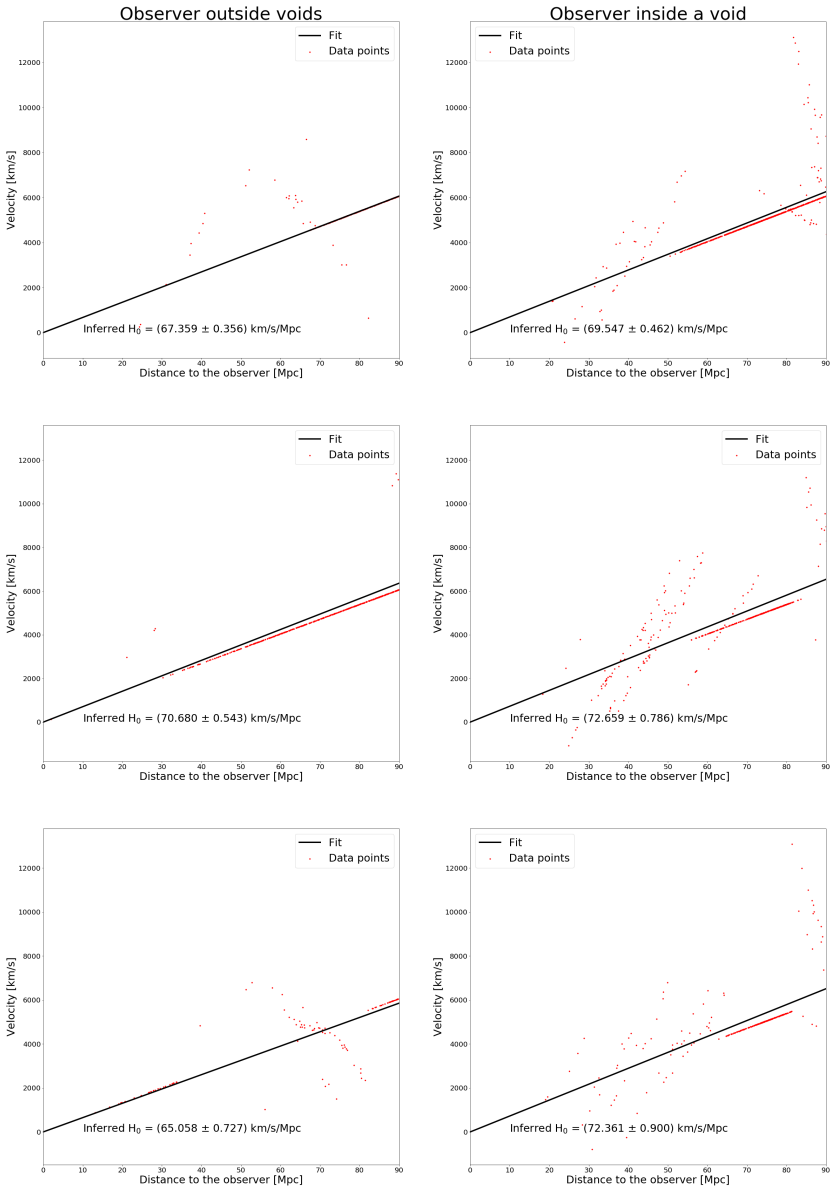

Figure 5.2: Radial velocity - distance relations. On the left from an observer not in a void, in three directions. on the right for an observer in a void, in three directions. For all the plots, the red dots represent the data points and the black line represents the fit through them. The slope and the error in the slope can be seen on each plot.

From these figures it can also be seen that the fit works, meaning that it was possible to move on to a statistical analysis.
The goal of this analysis is to analyze the spread in values of H_0 reached from various lines of sight and to compare the values taken from inside and outside voids. To do this multiple positions were selected outside and inside voids, and from each of these positions lines of sight were taken in multiple directions. The result of this analysis can be seen in figure 5.3, where each histogram contains 1000 data points. Taking this many data points should eliminate the element of casualty, meaning that if there appears to be a consistent difference in inferred H_0 in the two kinds of starting points, with this many points it can be assumed that the difference exists.
These histograms are a useful tool to understand how being inside a void could affect the measurement of the Hubble constant, but also how voids, in general, can influence such measurement.
The spread in values is similar in both cases, but the distribution for the case of an observer not inside a void is much more peaked around the "real" values of H_0, whereas, in the case of an observer inside a void, the distribution is much wider. Moreover, on both figures, the values for the mean H_0 have been printed and it can be seen that in the first figure the mean value is much closer to the real value than in the second case. It can be noticed that an error has also been added to the value of H_0. This value, here and in subsequent plots, was taken as one standard deviation.
Another noticeable feature of these histograms is that the peak of the first histogram is quite clearly around the real value of the Hubble constant, whereas the second histogram appears to have two peaks, one around the correct value, albeit much smaller than in the first histogram, and another one shifted towards higher values. This means that, not only is finding values of H_0 different from the real value more likely when the observer is inside a void than when the observer is outside, but it is actually more likely that an observer inside a void would measure a higher value of H_0 than measuring the real one.

5.1 Various void clustering

It was also of interest to investigate how different distributions of voids in space could affect the measurements of H_0 both taken from inside and outside voids. For this reason, the same histograms that can be seen in figure 5.3 were also built for different distributions of voids.
For the histograms in figure 5.3 the voids were clustered using 10 parent points and 10 offspring points for each parent, so an interesting idea was going to the extremes of the possible clustering distribution. This is why this kind of analysis was performed on voids which were distributed using 2 parent points and 50 offspring points each and on voids which were distributed using 50 parent points and 2 offspring points each. The first distribution of the two is a very clustered distribution, with many voids overlapping, whereas the second distribution is more rarefied.

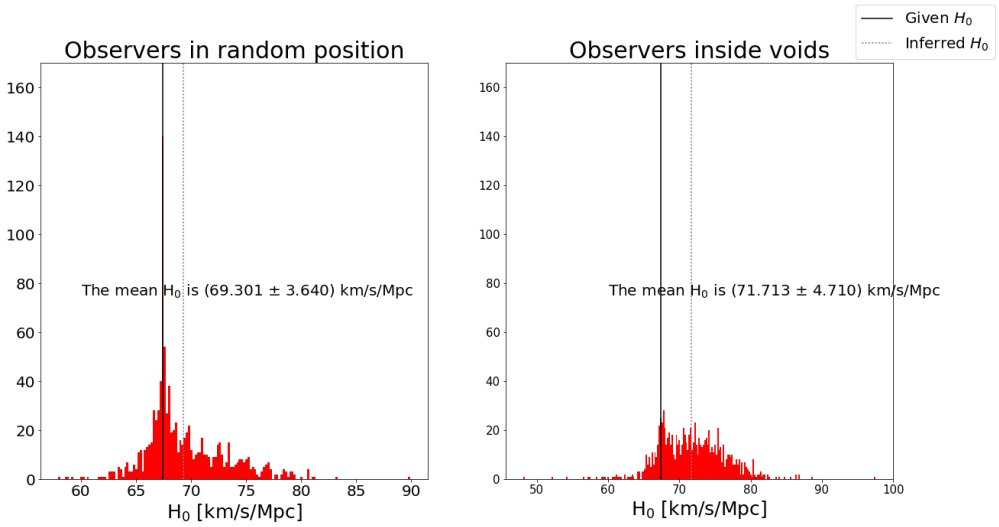

Figure 5.3: Histograms of inferred Hubble constants. One the left: Histogram of values for H_0 inferred from starting positions outside of voids. On the right: Histogram of values for H_0 from starting positions inside voids. Each histogram contains 1000 data points. The values of the mean values of H_0 with the error has been added to each figure.

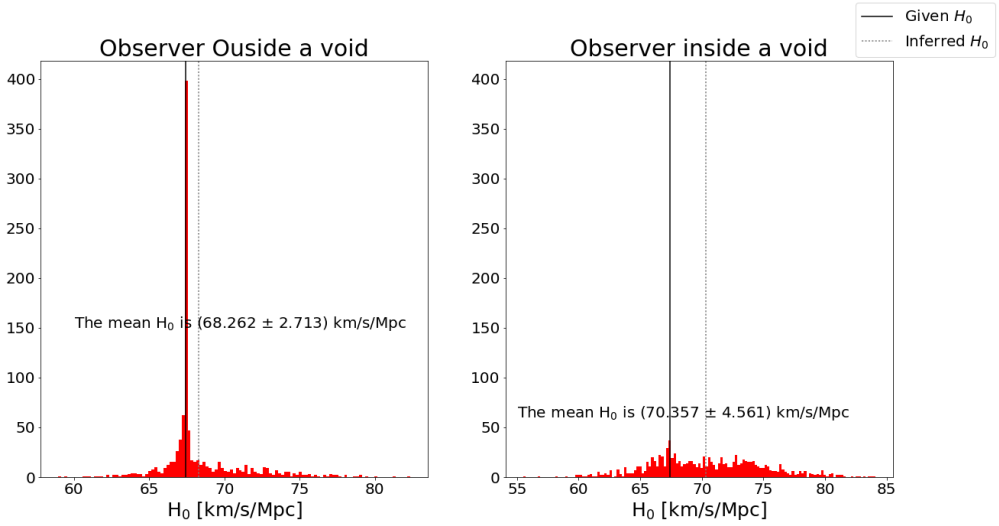

Figure 5.4: Histograms of inferred Hubble constants. The distribution of voids for this analysis was created from 2 parent points and 50 offsprings for each parent. On the left: Inferred H_0 when the observer is not inside a void. On the right: Inferred H_0 when the observer is inside a void.

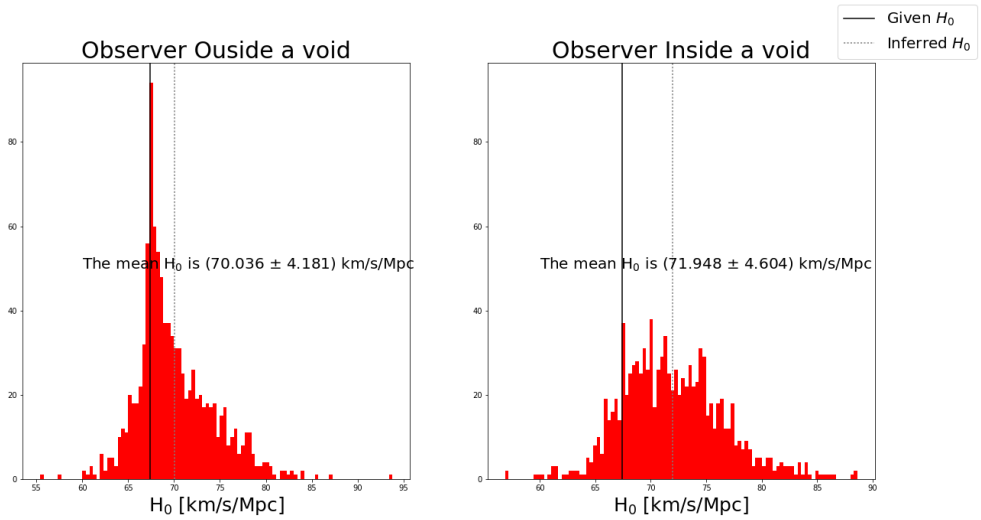

Figure 5.5: Histograms of inferred Hubble constants. The distribution of voids for this analysis was created from 50 parent points and 2 offsprings for each parent. On the left: Inferred H_0 when the observer is not inside a void. On the right: Inferred H_0 when the observer is inside a void.

As can be seen in figure 5.4, when the voids are very clustered and overlapping the resulting distribution of H_0 will be shaped similarly to that in figure 5.3, as expected. When the observers are outside of voids, the distribution is very peaked and has very small wings and when the observers are inside the voids a small peak can be seen around the real value, with very prominent wings.
However, the two figures have noticeable differences. The Gaussian distribution for the observer in a void histogram in figure 5.4 does look flatter than the one in figure 5.3 and the Gaussian for the observers outside of voids has a much bigger peak. The same number of data points has been used for all the histograms, so what can be inferred from these features is that it's more likely in the case of figure 5.4 to find the real value of H_0 when observing from outside voids.
Something else to notice in figure 5.4 is that the mean value of H_0 found from the histogram on the left is much closer to the true value than the value found from the same kind of histogram in figure 5.3 and it also has a smaller error. This is probably due to the fact that having voids so clustered leaves a lot of lines of sight in which there are no voids, so the real value of H_0 will be found in those cases.
In figure 5.5 the histograms for the inferred values of H_0 for a rarefied distribution of voids can be seen. The spread in this figure is similar to that of figure 5.3 but bigger than that of figure 5.4. What is important to notice is

that the Gaussian for values inferred by an observer outside of voids is wider than in the other two cases and the wings are very prominent in this case. This is because, having so many rarefied voids, it is very likely that any line of sight will pass through a void, even when taken form an observer outside a void. In fact, in this case, the peak around 67.4 is not as big as in the other two histograms, but the curve is smoother. Because of this, the mean of this distribution is further away from the real value than in the other two cases, and it has a much bigger error.
It can also be noticed that the distribution of values found by observers inside voids is similar in shape and mean value to that of figure 5.3 and that the mean of both of them is higher than that of figure 5.4. This is because, in the case of figure 5.4, all the void points are relatively close to each other so there is the chance to have a line of sight almost clear of voids if an observer is in a void at the edge of the cluster. Instead in the other two cases, the voids are all over the place so it is difficult to find such a clear line of sight.

5.2 Discussion on bubble model results

From this model, it can be seen that in such a simple scenario, the influence of voids in the radial velocity - distance relation is evident. Such an influence can already be seen when looking back at figure 5.2, in the individual lines of sight, but it becomes more evident when surveying the whole sky.
The influence of voids can be seen not only when the observer is inside a void but also when there are many voids around the observer, especially if the voids are very scattered around the observer, as figure 5.5 shows.
Overall this model shows that the influence of voids on the value of H_0 suggested earlier in the thesis could be a good candidate as the reason behind the lack of uniformity in the measured Hubble constant from Earth. This hypothesis is thus in need of a more realistic and in-depth analysis, which will be performed using a ΛCDM simulation.

Chapter 6

ΛCDM cosmology: Voids and the measured Hubble parameter

Here an N-body simulation based on ΛCDM cosmology will be used to get a deeper understanding of how voids might influence the inferred Hubble parameter. First, an introduction to ΛCDM cosmology will be given, then the N-body simulation used will be presented, together with some plots showing the matter distribution in some slices of the simulation. Next, the MMF/Nexus algorithm used for the identification of structure in the simulation will be explained.
From the N-body simulation, the dark matter halos will be identified, so a small introduction on dark matter will be given and then an explanation of why dark matter halos are important and how they were found from the simulation will be provided.
Lastly, the method used for analyzing the radial velocity - distance relation will be explained.
The results of this analysis will be presented in the next chapter.

6.1 ΛCDM Model

The ΛCDM model is an improvement on the Big Bang theory and it assumes that most of the physical substance in the universe is slow moving, cold dark matter (GaBany). Dark matter is invisible to the eye since it does not emit electromagnetic radiation nor it interacts with light, nonetheless, its existence is known due to the gravitational effect it has on visible matter (CERN). There are many candidates for these missing particles, but unfortunately, due to the impossibility of direct observations of dark matter, none of the theories have ever been confirmed.

The ΛCDM model has another part other than the cold dark matter, and it is indicated by the Λ. Here Λ indicates dark energy, which is a hypothetical force that appears to be accelerating the expansion of the Universe (GaBany). A peculiar aspect of dark energy is that it seems to be distributed evenly both in space and time, meaning that the expansion of the Universe does not dilute its effects. This also means that dark energy does not have any local gravitational effects, but only global, affecting the Universe as a whole (CERN).
In figure 6.1 a representation of a ΛCDM simulation and its comparison to real world observations can be seen. It is clear that the simulation looks very similar to the real world observation, proving the ΛCDM model to be a good representation of reality.

6.2 N-body Simulation

In figure 6.2 2 slices taken from the ΛCDM N-body simulation that will be used are plotted. The slices are 0.5 Mpc thick and the structure is quite clear. Some overdense and some almost empty region can clearly be seen. This kind of structure becomes even more clear in figure 6.3, where 4 zoomed-in slices of the same simulation can be seen. The difference between the two figures is that in figure 6.3 the slices are 5 Mpc and zoomed-in to only be 50 Mpc long per side, instead of being as big as the box and 0.5 Mpc thick. This allows for a better view of the cosmic web structures. For example, a lot of structure, probably a filament, can be seen both in the top right and in the bottom left figure.
This kind of structure is what will be identified by the Nexus/MMF algorithm, as will be better explained in the next section.
Very important for this thesis is the velocity of all these particles, which could influence the inferred Hubble constant. The velocity field for the N-body simulation can be seen in figure 6.4. Here it can be seen that the arrows are pointing toward high density regions and away from low density regions, confirming what that matter flows out of voids.

6.3 MMF/Nexus

The Multiscale Morphology Filter (MMF) is a method for automatically segmenting the cosmic structure into walls, filaments, and clusters. The formalism classifies the matter distribution on the basis of the local variation in the density field, velocity field, and gravitational field (Libeskind et al., 2018). It subsequently uses a series of filters that identify structure in a scale independent manner (Aragón-Calvo et al., 2007).
The final outcome of the Nexus/MMF algorithm is a field in which at each location it is specified what structure was found (Libeskind et al., 2018).
This method is very useful because it can recognize structure of different sizes, which is especially noticeable when analyzing clusters (Aragón-Calvo et al.,

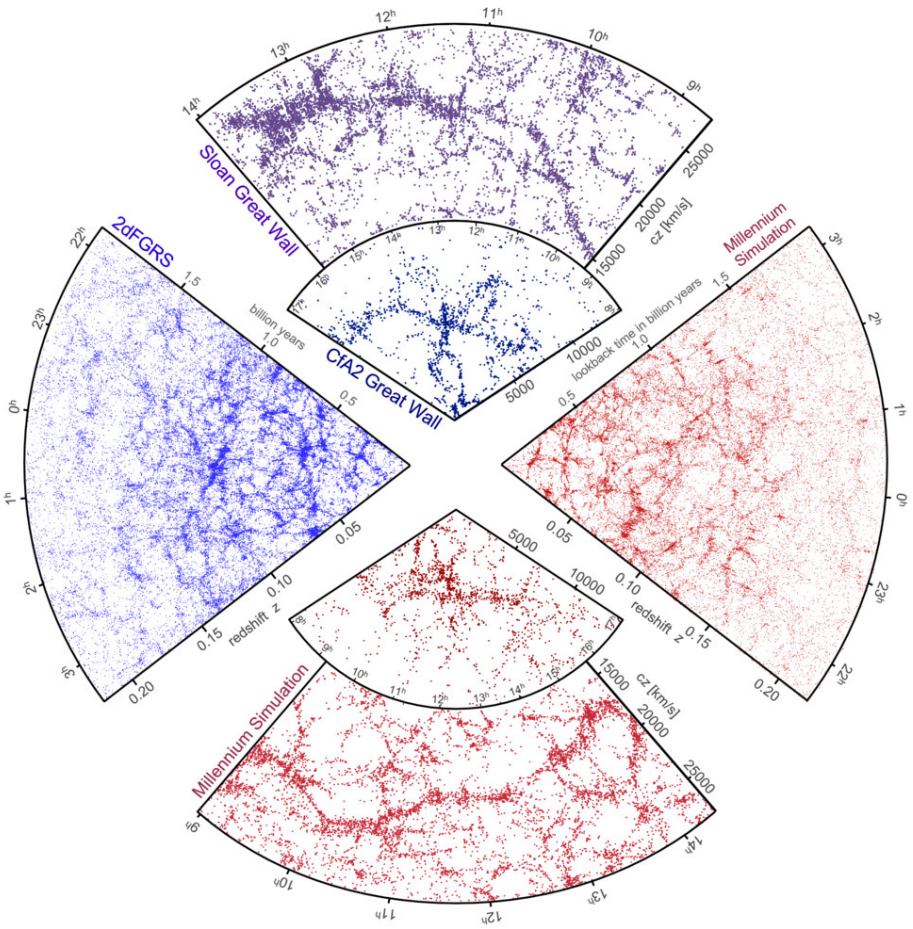

Figure 6.1: ΛCDM simulation and the real world. Here a comparison between the Millenium Simulation, a ΛCDM simulation and the real world can be seen. The resemblance between the simulation and the real world is clear. Lemson and Virgo Consortium (2006)

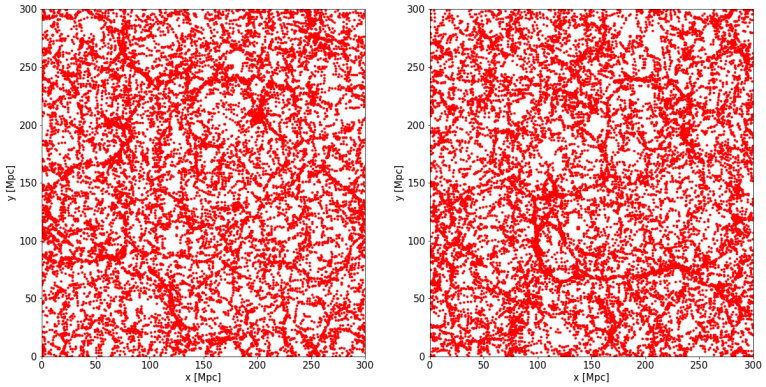

Figure 6.2: Slices through N-body simultion. Two slices taken through the ΛCDM N-body simulation. This shows the particle distribution. The slices are 0.5 Mpc thick.

2007).
Before the MMF method can be applied, the density field needs to be presented as a continuous function, instead of a collection of points. This is needed because the MMF method needs to use first and second derivatives of the field values (Aragón-Calvo et al., 2007). This can be done because it is assumed that the points are sampling an underlying density field, so this is only a matter of understanding what this distribution looks like. This can be done by using the Delaunay Triangulation Field Estimator ("DTFE") reconstruction of the density field (Aragón-Calvo et al., 2007). This method was used because it optimizes the continuous density field, retaining all visible features (Aragón-Calvo et al., 2007).
Something to keep in mind is that the MMF method is not a void finder, it is only able to recognize walls, filaments, and nodes (Aragón-Calvo et al., 2007). However, for the sake of this thesis, anything that MMF was not able to categorize as either of the three features, was assumed to be a void.

6.4 Dark matter

Dark matter is undetectable since it does not emit electromagnetic radiation nor it interacts with photons (GaBany). However, its existence can be identified from the gravitational effect it has on visible matter. Since it cannot be observed directly, it is impossible to know what it really is, but there are many theories regarding that. What dark matter actually is made of is not relevant for this thesis, what is relevant is that dark matter influences visible matter in noticeable ways.

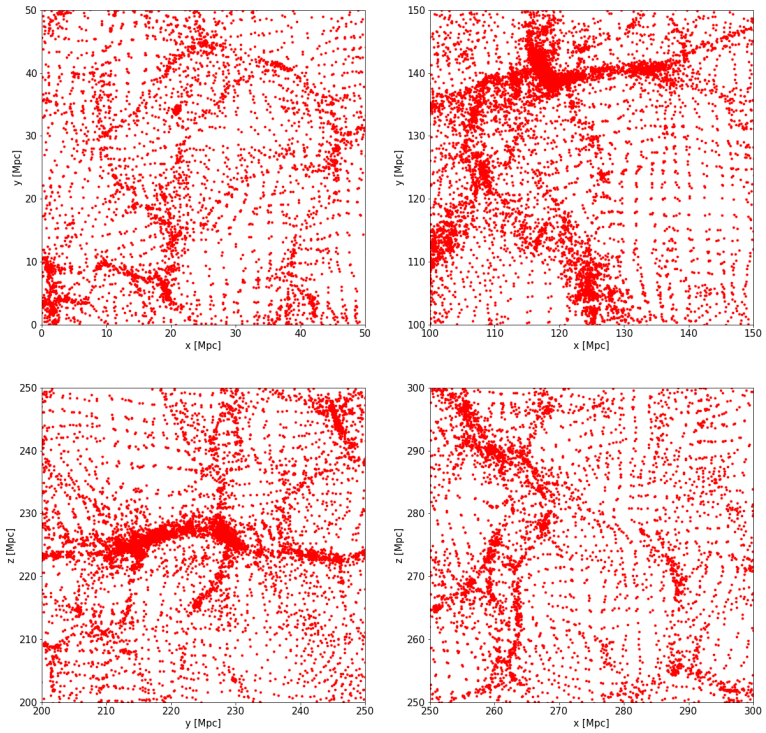

Figure 6.3: Zoomed-in slices through N-body simulation. Zoomed-in slices taken through the ΛCDM N-body simulation, to show the structure more in depth. The slices 5 Mpc thick and zoomed-in to have sides of 50 Mpc.

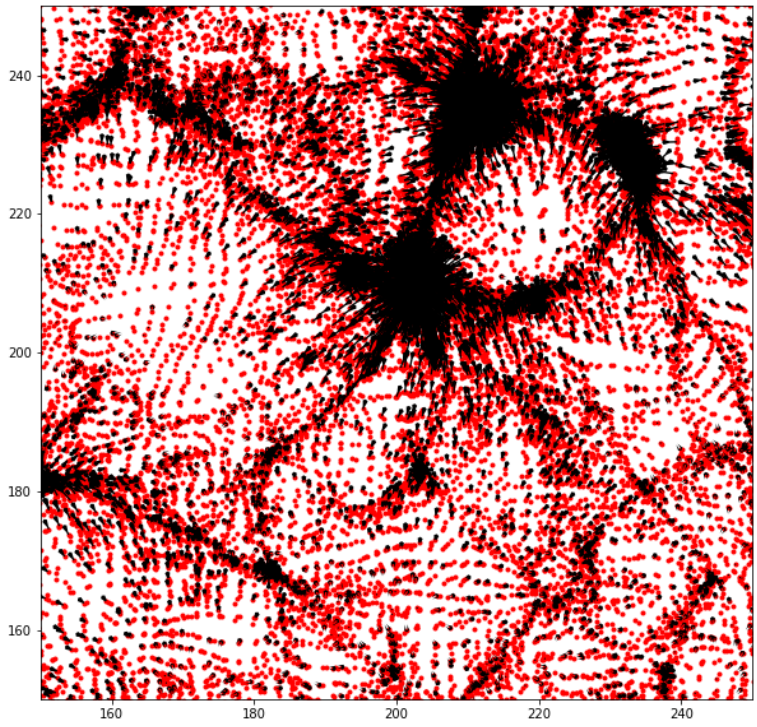

Figure 6.4: A slice taken through the ΛCDM N-body simulation, together with the density field, represented by the arrows.

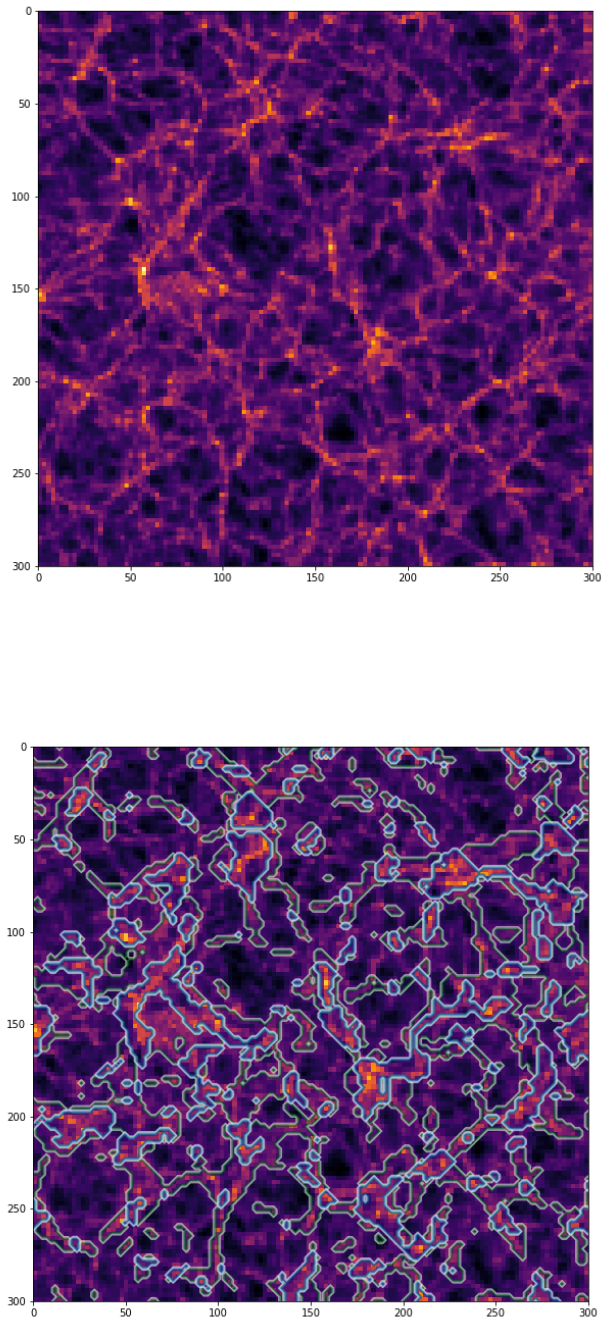

Figure 6.5: Density field. On the left: DTFE image of a slice through the N-body simulation used in this work. On the right: Same slice with MMF identification of features added.

The particles in the ΛCDM simulation represent the dark matter distribution, but dark matter is invisible, it can only be seen from its effect on other matter, so this distribution is also representing all the matter.
In this dark matter distribution, structure forms. For example, galaxies forms inside clumps of dark matter called halos.

6.5 Dark matter halos

Dark matter halos are important because they are the birthplace of visible galaxies (Behroozi et al., 2013). Dark matter halos surround galaxies and clusters of galaxies, so finding halos is the same as finding galaxies and clusters.
Dark matter halos were studied instead of galaxies because modeling entire galaxies would be too time and resource consuming, and out of the scope of this thesis. However, it is still interesting to know how galaxies behave in this model, if their expansion is influenced by voids and looking at dark matter halos allows for the same result, but reached more simply.
To recognize the dark matter halos from the N-body simulation, the rockstar pipeline is used.
The approach of the pipeline is based on an adaptive hierarchical refinement of friends-of-friends groups in six phase-space dimensions and one time dimension, which allows for robust (grid-independent, shape-independent, and noise-resilient) tracking of substructure (Behroozi et al., 2013).
As a first step, the algorithm finds overdense regions that will then be analyzed. Then, for each group, particle positions and velocities are divided by the group position and velocity, to normalize them. A linking length is then chosen such that at least 70 % of the group's particles are linked in subgroups. This process is repeated for every subgroup.
Once all the substructures have been found, seed halos are placed in the lowest substructure level and points are hierarchically assigned to the closest seed halo. Once all particles have been assigned, unbound particles are removed and properties are calculated.
Once the dark matter halos have been identified, lines of sights are taken from random positions in the different features, in the same way it will be done for the N-body simulation.
At first, all the clusters will be analyzed, then another analysis will be performed, this time only on halos with mass higher than $10^{10} M_{\odot}$, as those are in the same order of magnitude or heavier than the Milky Way.
In figure 6.6 the spatial distribution of the halos present in two 15 Mpc thick slices can be seen. This was added to give an idea of what will be explored later on.
Moreover, in figure 6.7 the spatial distribution of halos only with $M > 10^{10} M_{\odot}$ (top figures) and $M > 10^{12} M_{\odot}$ (bottom figures) have been plotted.
What can be seen here is that very massive halos live in very overdense areas, whereas underdense areas only have not so massive halos. This was an

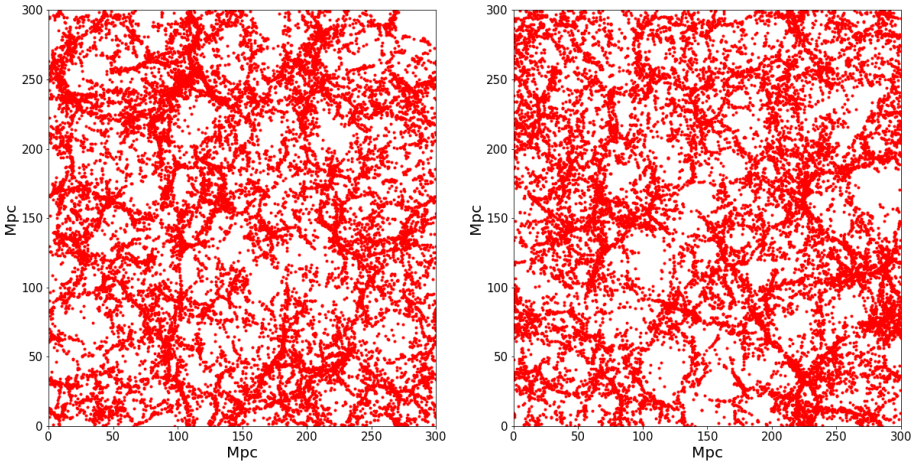

Figure 6.6: Positions of halos in two 15 Mpc thick slices

expected result, but their spatial distribution is still interesting to see.
Once again, in figure 6.8 we can see the velocity field in one slice of the simulation, due to the velocities of the single halos. Just as in figure 6.4 here we can see a flow of matter towards high density regions and away from underdense regions, as expected.

6.6 Method for taking lines of sight

After the structures and the dark matter halos were identified, lines of sight were taken from each kind of structure, in a similar way to what was done in the bubble model. To do this, first, it was necessary to write an algorithm that would identify which points belonged to what cell in the grid. This was necessary because Nexus works on a grid basis, which means that it identifies which grid cells belong to each feature. However, the lines of sight need a starting point which needs to be exactly a point, thus the need for such an algorithm. Once this was done, multiple lines of sight were taken starting from random points in each structure.
The lines of sight were taken in a way that is similar to the method used for the bubble model but with some adjustments.
Firstly, the points in the simulation were sampled, only one point every 25 was taken into account when investigating the radial velocity - distance relation. This was done to allow the code to run faster, while still reaching representative results. Without this step, taking 1000 lines of sight, starting in each feature, to build the histograms, would be too time consuming.

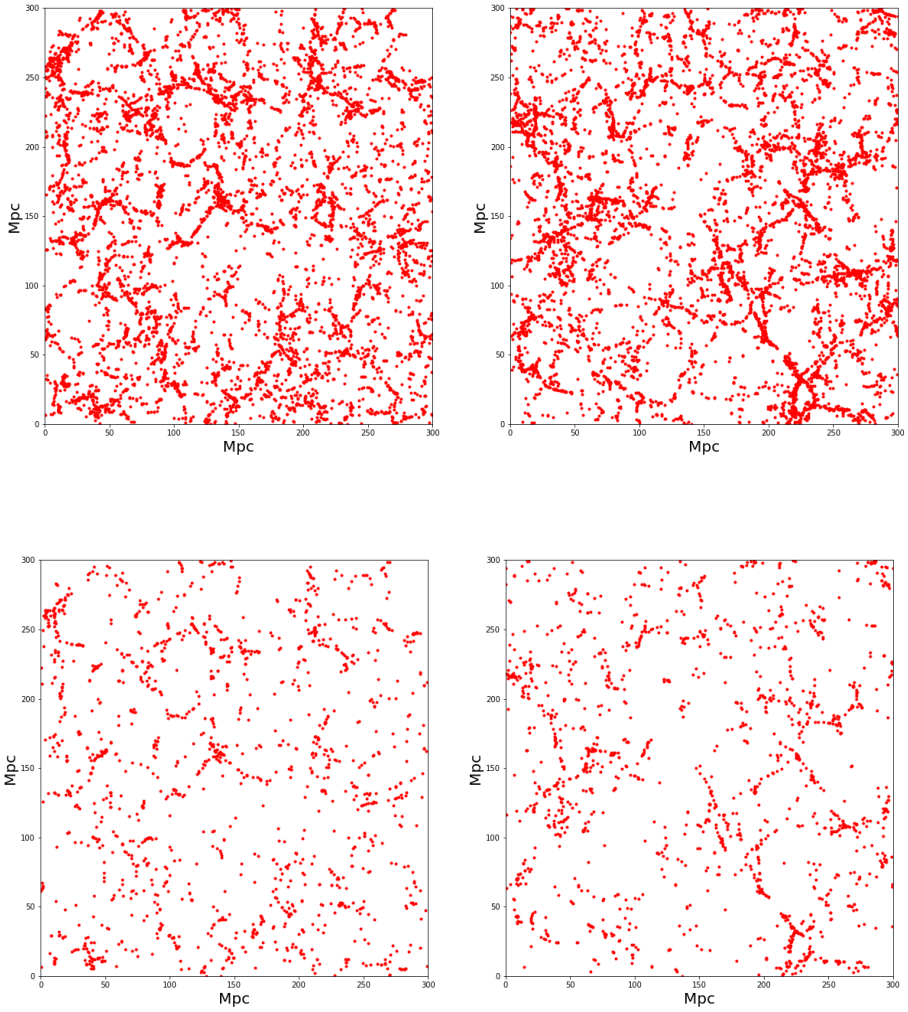

Figure 6.7: Positioning of halos of certain mass. On the top: Two slices which only include halos with mass $> 10^{10} M_{\odot}$. On the bottom: Two slices which only include halos with mass $> 10^{12} M_{\odot}$. All the plots are in the same 2 slices, so the plots on the left side belong to the same slice and the plots on the right belong to the same slice.

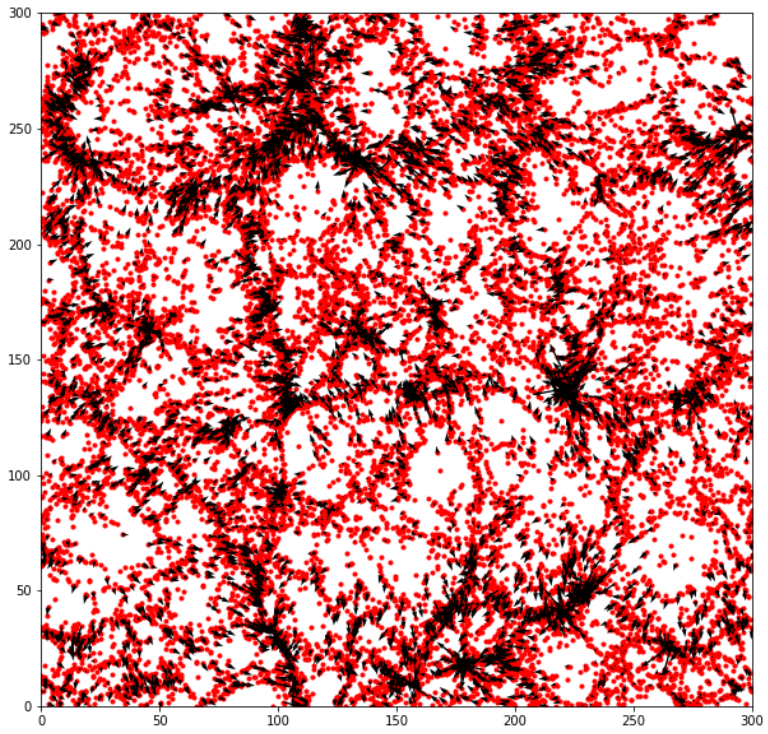

Figure 6.8: Velocity field in a slice. A slice showing the position of the dark matter halos together with their velocity, represented by the arrows.

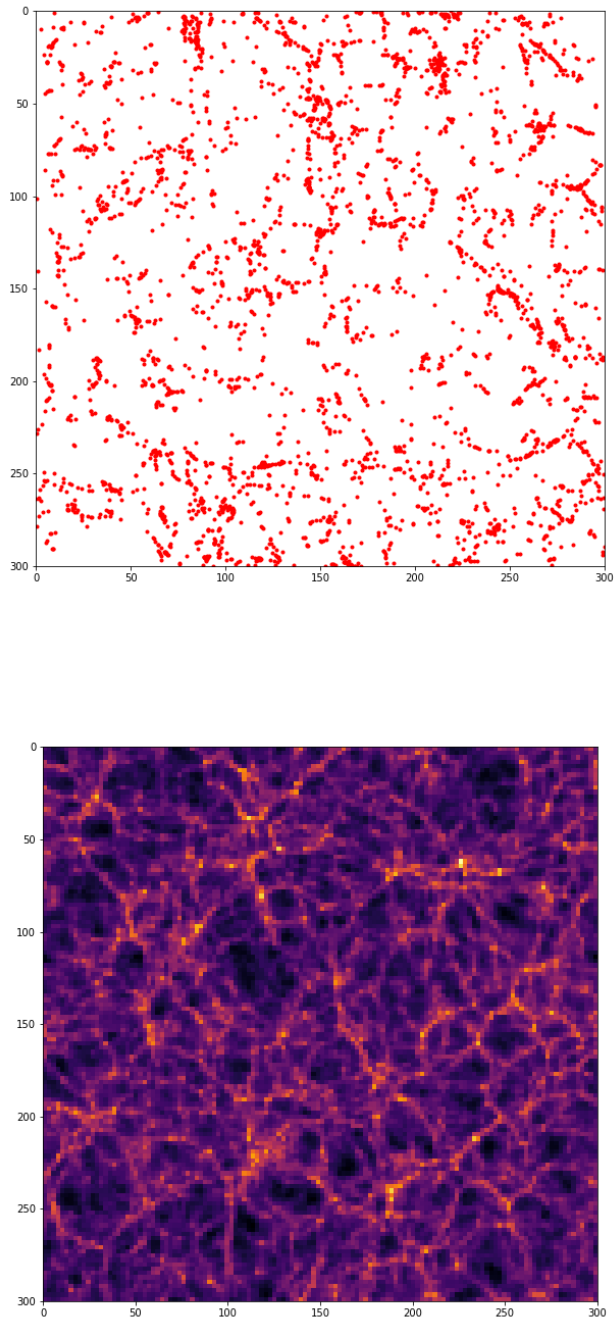

Figure 6.9: Comparison between density distribution and dark matter halos. Here a comparison can be seen between the density distribution and the spatial distribution of dark matter halos in the same slice of the simulation.

Next, to avoid running into artifacts due to the boundary conditions, the lines of sight were only made to be 250 Mpc long. Since this cone is much longer than that in the previous model, its radius to height relation was chosen to be 0.05. A smaller value wouldn't be possible due to the fact that not all points are being used so a smaller cone would not encounter enough points to have a sensible fit.
Another adjustment that was made with respect to the bubble model is that to find the fit, weighted linear least squares was used, with weights being $\frac{1}{r^2}$. This allows for point close to the observer to weigh much more heavily in the fit than points far away. If this way of fitting was not used, the fit would be too influenced by the peculiar velocity of structure farther away, as using a cone means that far away structures are more heavily sampled.

Chapter 7

Results of ΛCDM simulation

In this chapter, the results of the radial velocity - distance analysis of the ΛCDM simulation are presented. First, the results of the N-body simulation and then the data from the analysis of the dark matter halos will be presented. A selection of halos based on mass was also performed, and the results of the analysis of the radial velocity - distance relation of that selection of halos will be presented.
All these results will also be compared to each other, for a deeper understanding of their meaning.

7.1 N-body Simulation

Firstly, roughly following what has already been done in the previous model, individual lines of sight with starting points in the various features were compared. This comparison can be seen in figure 7.1. Already from these plots, a substantial difference with the previous model can be seen. In this simulation all the particles have a peculiar velocity, not only those in voids, thus, much more structure can be seen when plotting radial velocity against distance. For example, in figure 7.1, in the top left figure, a stripe can be seen at around 150 Mpc, which clearly indicates the presence of a cluster. The same kind of structure can also be seen in the bottom left figure, at around 200 Mpc.
Similarly to what was already done in the bubble mode, 1000 lines of sight were taken from random points in each feature and the inferred Hubble constant for each line of sight was plotted in a histogram. These histograms can be seen in figure 7.2. Unfortunately in these histograms such a striking difference between voids and other features, as was seen in the bubble model, is not present.
It can be seen that the histograms from observers in voids, walls, and filaments are quite similar. The only difference can be seen in the histogram from

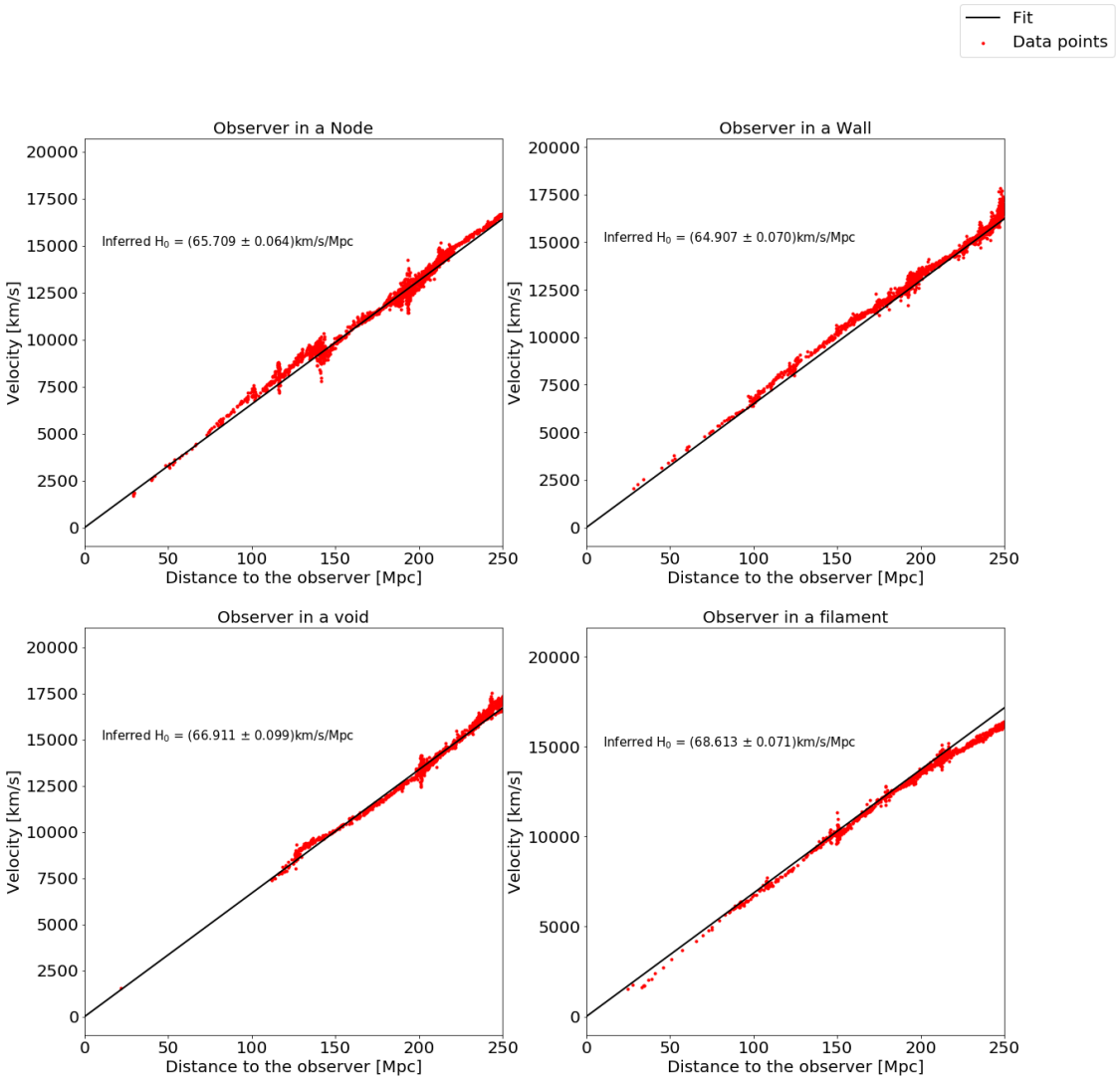

Figure 7.1: Here the comparison between lines of sight taken from different features in the N-body simulation can be seen. The peculiar velocities are much more prominent here than they were in the bubble model, leading to much more structure being visible in these plots.

observers in nodes. This histogram is a bit less peaked and is a bit wider than the other three.
Something else to notice is the errors in the mean H_0 value for each histogram. This value, just as was done in the bubble model, was chosen to be the standard deviation. It can however be seen that the histogram for the observer in the nodes does not have the biggest error, even though it looks like it has the most significant wings. This is probably because the histogram for the observers in filaments has substantially more outliers. Values below 50 km/s/Mpc and above 100 km/s/Mpc can be seen here but not anywhere else.
Figure 7.2 can also be compared to figure 5.3. What can be noticed from this comparison is the influence that the peculiar velocity of all particles has on the histograms. In figure 5.3 there is one clear spike in the left histogram, exactly at 67.4 km/s/Mpc and flatter wings around it. This is because if the line of sight does not encounter voids the inferred H_0 will be exactly 67.4 km/s/Mpc. Instead, in the case of figure 7.2, there is still a spike around 67.4 km/s/Mpc, but it is not just one bin, exactly at that value, being much bigger than the rest, it is a more smooth Gaussian, albeit quite thin.

7.2 Dark matter halos

For a more realistic study of the radial velocity - distance relation, dark matter halos were investigated. The procedure used was the same as that used for the N-body simulation, with the difference that instead of having many particles, each cluster of galaxies or galaxy was only identified by one point. In figure 7.3 four sample lines of sight can be seen. These lines of sight were taken in the same way as for the N-body simulation.
Comparing figure 7.3 to figure 7.1 it can be seen that it looks like less structure is present in figure 7.3 than in figure 7.1. This is because galaxy clusters are often in the same dark matter halos, meaning that what would be noticeable structure, represented by multiple points in figure 7.1, is represented by a single point in figure 7.3. It also looks like there are fewer data points in figure 7.3 than in figure 7.1, for pretty much the same reason. The cone size has not changed between the two figures, but what used to be many different points in figure 7.1, is now just represented by one single point. In figure 7.4 the histograms representing the inferred value of H_0 starting from the different features can be seen. Of course, also these lines of sight only include dark matter halos. Here we can see results similar to what was reached using the N-body simulation. All the histograms look similar, there is not a striking difference in inferred H_0 between observers placed in different features.
Comparing figure 7.4 to figure 7.2 it can be seen that the histograms are mostly similar except for the observer in nodes histogram. The nodes histogram in figure 7.4 is much more peaked than the other one, even though in figure 7.4 that histogram is still the one whose mean is further away from the given value, compared to the other histograms in the same figure.

7.2.1 Selection of halos

For this section, only halos with mass similar or bigger than that of the Milky Way were selected. This was done to add another layer to this investigation in the role of voids in the calculation of H_0. Realistically, anything much smaller than that, if far away, might not be seen.
Once again 1000 lines of sight were taken from each feature in the cosmic web and the results have been plotted in figure 7.5. These results are not very different from the results in figure 7.4, which is reasonable since the lines of sight are taken through almost the same set of data. There are some small differences to notice, especially in the wings. For example, one can notice that the walls histogram in figure 7.5 looks like it has more substantial wings than that in figure 7.4.
While the means stayed very similar between figure 7.4 and figure 7.5, it can be noticed that the nodes histogram appears to have a higher peak in figure 7.5. This peak is just below the given value of H_0.

7.3 Discussion on results of ΛCDM simulation

As was already pointed out before, in two cases filaments have very big outliers. Filaments can be found on the edge of voids so this behavior might be due to the presence of voids.
Overall, though, from figures 7.2, 7.4, and 7.5, one can find very little evidence for voids being the reason for the difference in inferred H_0 values.
The histograms with values taken from the different feature look quite similar in all cases and the means of all those histograms are very close to the given H_0 value, and all of them are comfortably within error margins.

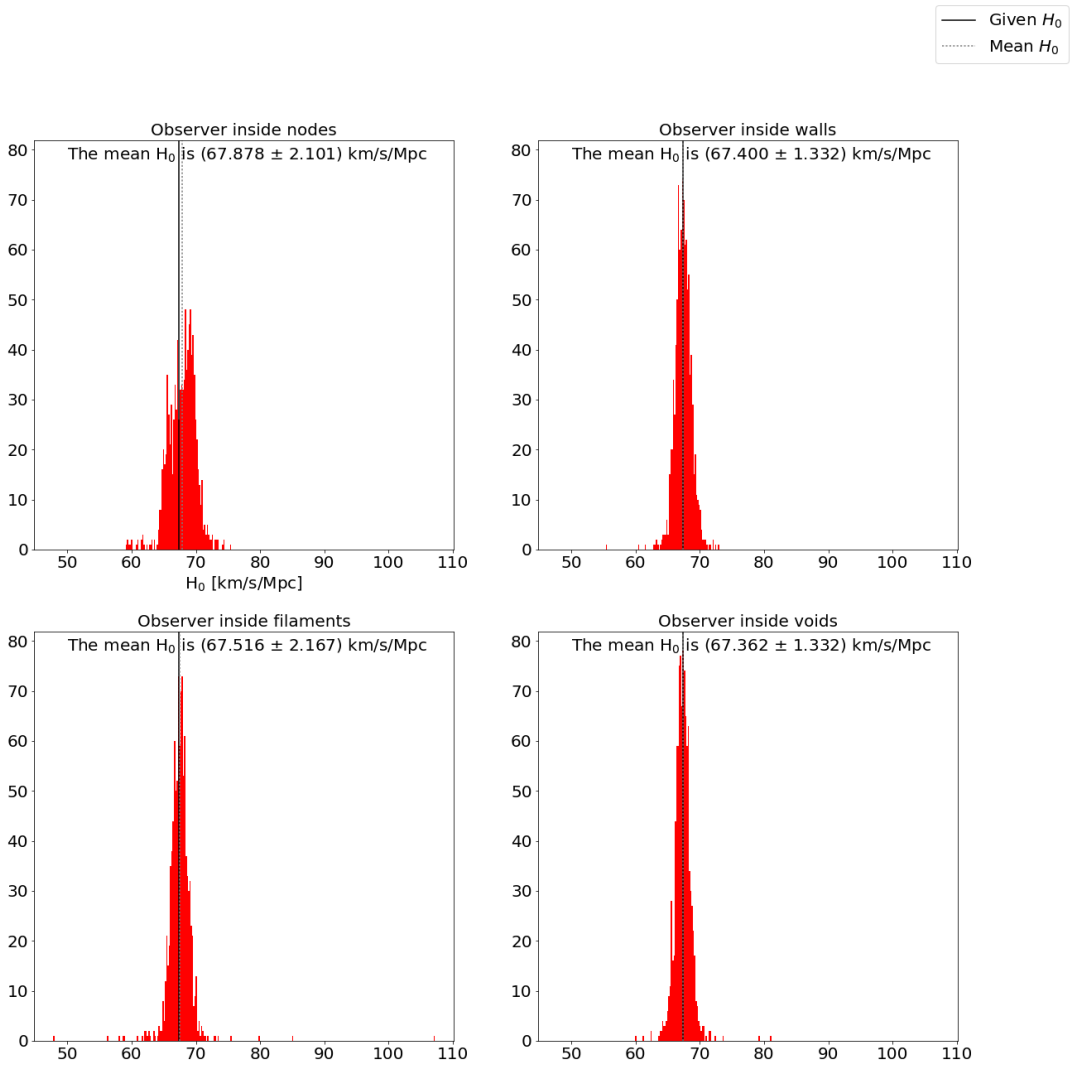

Figure 7.2: H_0 values inferred from random positions and directions in the different features in an N-body simulation. The mean value for each histogram and the standard deviation was added to the figure itself. Each histogram contains 1000 data points. The solid black line represents the given H_0 value, so 67.4 km/s/Mpc and the dotted line represent the mean of the gaussian.

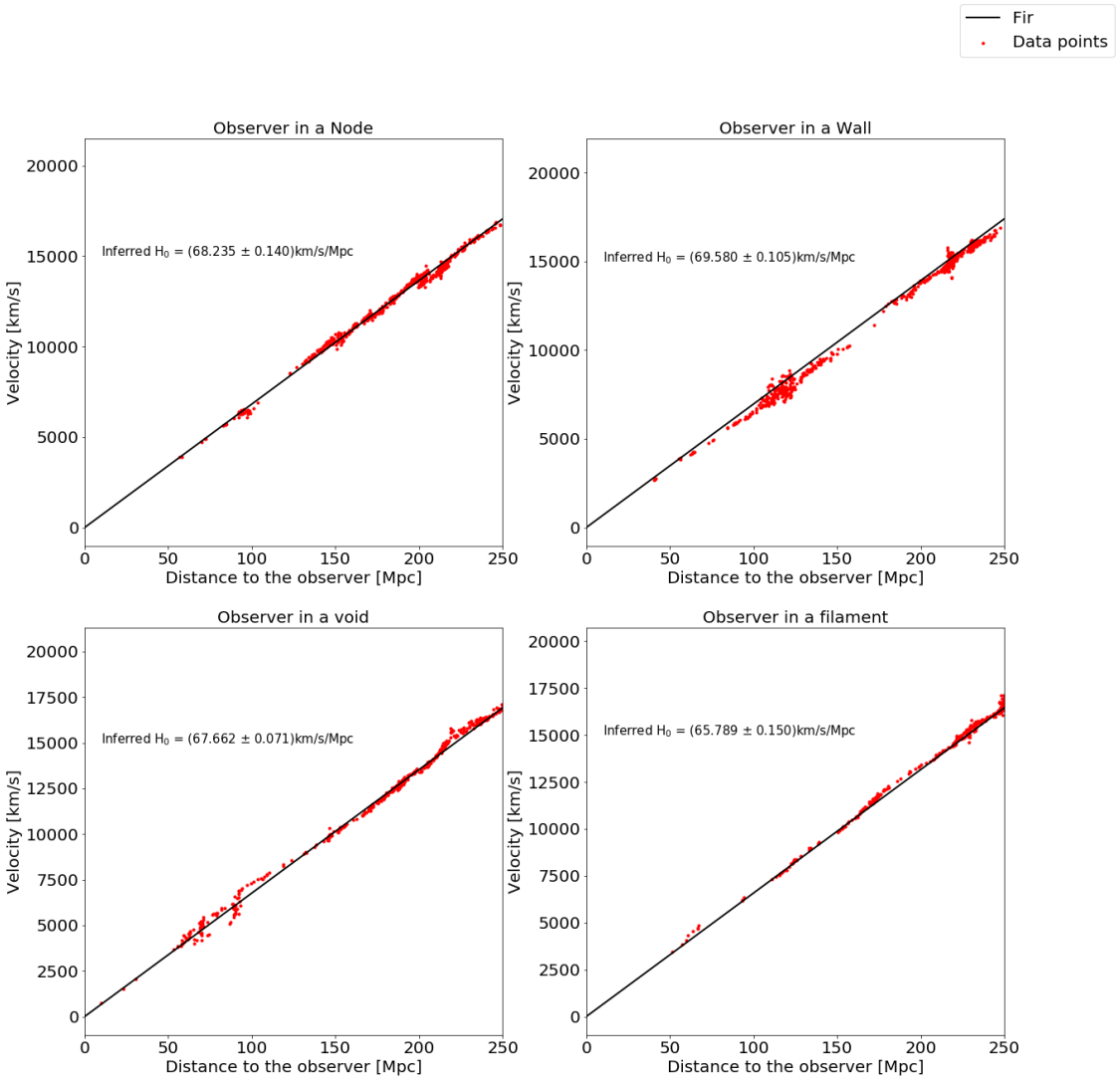

Figure 7.3: Here the comparison between lines of sight taken from different features, only including the velocities and positions of dark matter halos, can be seen. Here galaxies are only represented by one point each, so much less structure is visible than in the N-body simulation.

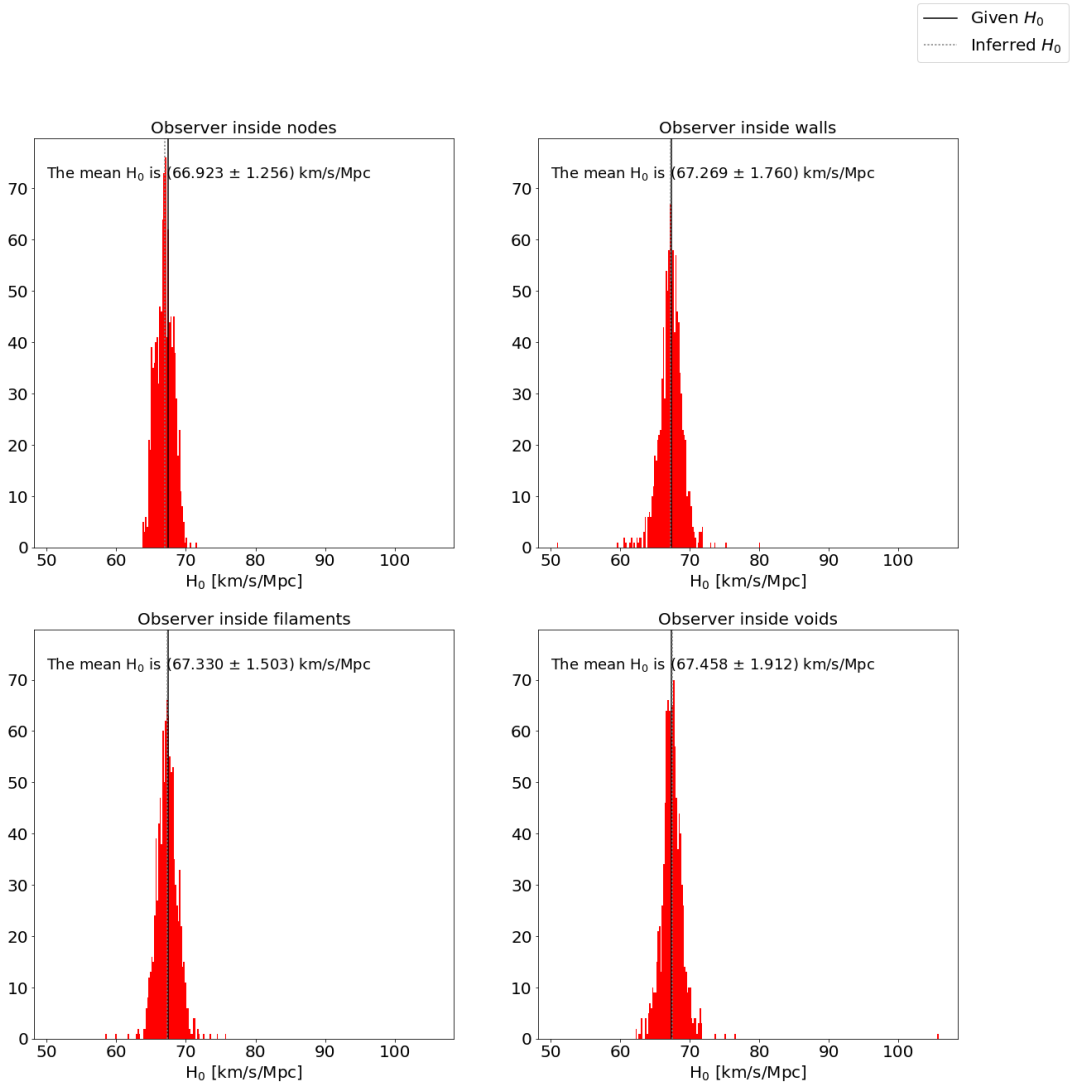

Figure 7.4: H_0 values inferred from random positions and directions in the different features, only including dark matter halos. The mean value for each histogram and the standard deviation was added to the figure itself. Each histogram contains 1000 data points.The solid black line represents the given H_0 value, so 67.4 km/s/Mpc and the dotted line represent the mean of the Gaussian.

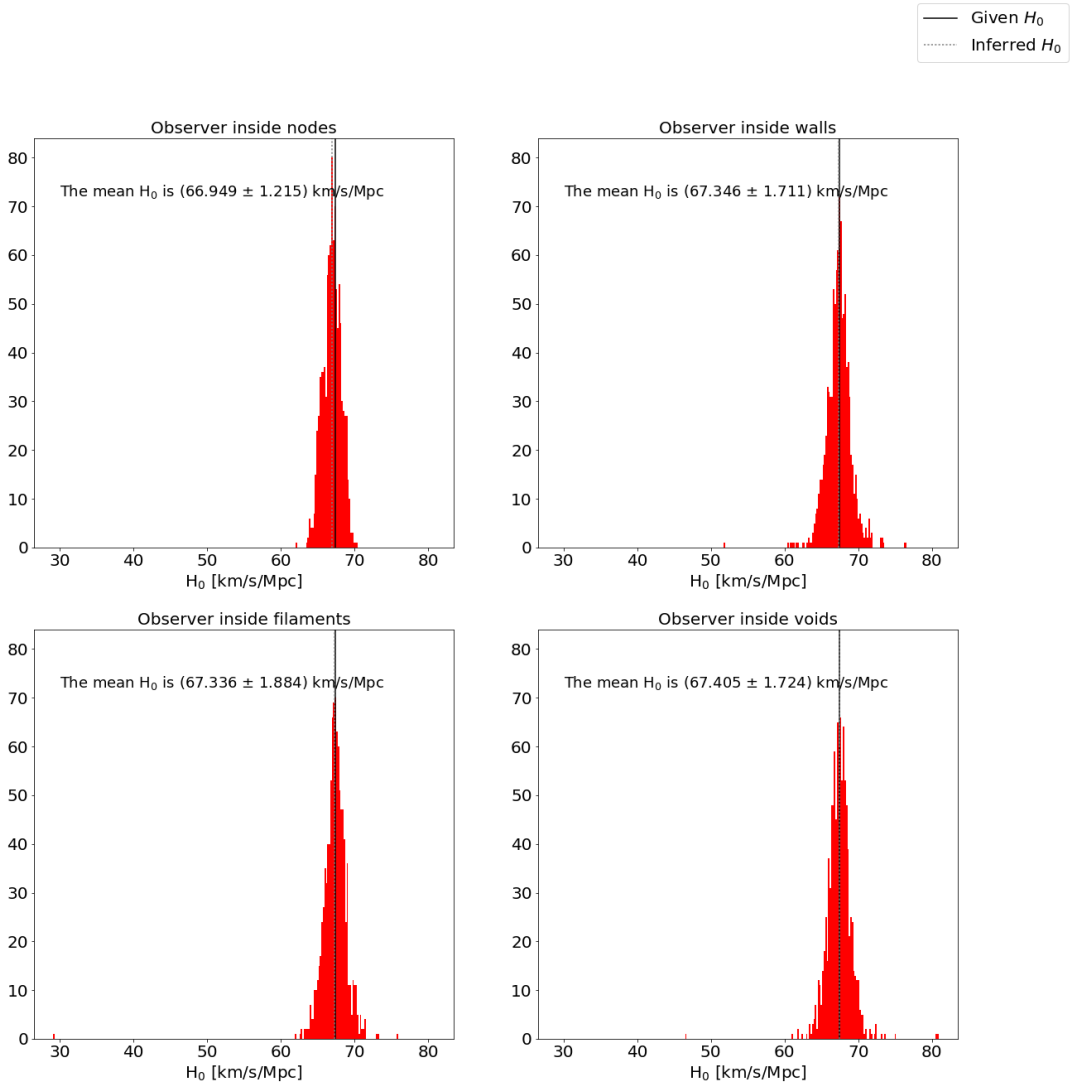

Figure 7.5: H_0 values inferred from random positions and directions in the different features, only including dark matter halos with $M > 10^{10} M_\odot$. The mean value for each histogram and the standard deviation was added to the figure itself. Each histogram contains 1000 data points.The solid black line represents the given H_0 value, so 67.4 km/s/Mpc and the dotted line represent the mean of the Gaussian.

Chapter 8

Conclusion and improvements

8.1 Conclusion

This bachelor's thesis aimed to investigate the role that the presence of voids could have in the lack of uniformity in the measured Hubble constant values. Two models were used for this analysis, a simple one, and a much more complex ΛCDM simulation.
According to the first, very simple model, voids can be addressed as the cause of this lack of uniformity, especially if the observer is in a void.
Once the bubble model gave plausible and interesting results, the analysis was moved to the ΛCDM simulation. This analysis was performed in two steps. First, the simulation was analyzed as an N-body simulation, then the dark matter halos were identified and analyzed. In both cases, the results were much less clear cut. The difference in values of the Hubble constant measured from various elements of the cosmic web is almost imperceptible and those values are not very different from the value of H_0 added to the peculiar velocities when taking lines of sight.
Overall, a clear conclusion on the role of voids in the measurements of the Hubble constant cannot be drawn.

8.2 Comparison of results with literature

The idea behind this thesis was studying if the peculiar velocity of matter in voids could influence the measurements for the Hubble constant, especially in the case of the Milky Way being at the center of a void. This peculiar velocity would make the inferred Hubble constant higher than the real Hubble constant, as matter is streaming outwards from voids. This could lead to the discrepancy seen in real life, with the CMB value, the "real" value,

as a lower limit on the late Universe measurements. This is why the value of 67.4 km/s/Mpc was used as the "real" H_0 value during this thesis, as it is the most recent value reached from the Planck data of the CMB (Planck Collaboration et al., 2018).
The results reached in this thesis are not clear, and they were not expected to be. However, the results of the bubble model indicate that the influence of voids might be the reason of this discrepancy since the values reached with that model overlap with the values of SH0ES (Riess et al., 2019), that of the CCHP, who used the TRGB method (Freedman et al., 2019) and the value of HOLiCOW (Wong et al., 2020).
The result from the ΛCDM simulation, instead, agree with the "real" value of H_0, implying that voids might not actually play the expected role in this discrepancy. Of course, many astronomers would agree with this position, that voids do not cause the discrepancy and it is important to understand why that is.
No evidence of a sharp change in the Hubble constant, inferred from the distance - redshift relation of SNe Ia, which would indicate the presence of a void around the Milky Way, has been found at any redshift (Kenworthy et al., 2019). However, this result is heavily dependent on the cosmic distance ladder and thus very influenced by local structure, leading to quite high systematic error.
Others, instead, think that even if the Milky Way was at the center of a local void, this void would have to be too big to account for the tension seen in Hubble constant values. (Wu and Huterer, 2017).

8.3 Improvements

Of course, there is still space for further research and also for some improvements.
Probably the biggest improvement that could be done is on the bubble model. This model reached the expected conclusion, but it could be made more realistic and accurate.
When building the model, first the points that represent the background universe were created and uniformly distributed and then the voids centers were identified using the Neymann-Scott process. The already existing points were then deleted in a sphere around the voids centers and replaced with the points for the voids, with the correct velocity. This means that when there are overlapping voids, their points and their velocities will also overlap. This could lead to less accurate reading in case of overlapping voids.
This could be fixed by having points only be created for each void until halfway through to the next void and not in a sphere disregarding the existence of other voids. However, since the velocity of each point is dependent on the Δ of the void and on the radius, the halfway point is not exactly halfway but it should be a weighted average between the velocities of two overlapping voids. This was not done in this thesis as it is quite complicated and maybe out of

the scope of the project. Moreover, the bubble model was specifically built to be a very simple model, to give an idea of what results could be expected, and this improvement would not change the results substantially, so it was avoided.
Other than this point, it is worth mentioning that the MMF algorithm is not a void finder, but everything that was not categorized was assumed to be a void. This is probably not completely accurate, so using a void finder might be a way to expand this research and improve it.

Bibliography

M. H. Abitbol, J. C. Hill, and J. Chluba. Measuring the Hubble Constant from the Cooling of the CMB Monopole. , 893(1):18, Apr. 2020. doi: 10.3847/1538-4357/ab7b70.

M. A. Aragón-Calvo, B. J. T. Jones, R. van de Weygaert, and J. M. van der Hulst. The multiscale morphology filter: identifying and extracting spatial patterns in the galaxy distribution. , 474(1):315–338, Oct. 2007. doi: 10.1051/0004-6361:20077880.

P. S. Behroozi, R. H. Wechsler, and H.-Y. Wu. The ROCKSTAR Phase-space Temporal Halo Finder and the Velocity Offsets of Cluster Cores. , 762(2): 109, Jan. 2013. doi: 10.1088/0004-637X/762/2/109.

M. Cautun, R. van de Weygaert, B. J. T. Jones, and C. S. Frenk. Evolution of the cosmic web. *Monthly Notices of the Royal Astronomical Society*, 441 (4):2923–2973, 05 2014. ISSN 0035-8711. doi: 10.1093/mnras/stu768. URL `https://doi.org/10.1093/mnras/stu768`.

CERN. Dark matter. URL `https://home.cern/science/physics/dark-matter`.

Encyclopaedia Britannica. Georges lemaître. URL `https://www.britannica.com/biography/Georges-Lemaitre`.

W. Freedman et al. Final results from the hubble space telescope key project to measure the hubble constant. *Astrophys. J.*, 553:47–72, 01 2001.

W. L. Freedman, B. F. Madore, D. Hatt, T. J. Hoyt, I. S. Jang, R. L. Beaton, C. R. Burns, M. G. Lee, A. J. Monson, J. R. Neeley, M. M. Phillips, J. A. Rich, and M. Seibert. The Carnegie-Chicago Hubble Program. VIII. An Independent Determination of the Hubble Constant Based on the Tip of the Red Giant Branch. , 882(1):34, Sept. 2019. doi: 10.3847/1538-4357/ab2f73.

R. J. GaBany. The Formation and Evolution of Galaxies. URL `https://www.cosmotography.com/images/galaxy`$_f ormation_a nd_e volution.html$.

E. Gibney. Belgian priest recognized in hubble-law name change. URL `https://www.nature.com/articles/d41586-018-07234-y`.

J. P. Huchra. The hubble constant. URL https://www.cfa.harvard.edu/ dfabricant/huchra/hubble/.

IAU. IAU members vote to recommend renaming the Hubble law as the Hubble–Lemaître law. URL https://www.iau.org/news/pressreleases/detail/iau1812/?lang.

W. D. Kenworthy, D. Scolnic, and A. Riess. The Local Perspective on the Hubble Tension: Local Structure Does Not Impact Measurement of the Hubble Constant. , 875(2):145, Apr. 2019. doi: 10.3847/1538-4357/ab0ebf.

G. Lemson and t. Virgo Consortium. Halo and Galaxy Formation Histories from the Millennium Simulation: Public release of a VO-oriented and SQL-queryable database for studying the evolution of galaxies in the LambdaCDM cosmogony. *arXiv e-prints*, art. astro-ph/0608019, Aug. 2006.

N. I. Libeskind, R. van de Weygaert, M. Cautun, B. Falck, E. Tempel, T. Abel, M. Alpaslan, M. A. Aragón-Calvo, J. E. Forero-Romero, R. Gonzalez, S. Gottlöber, O. Hahn, W. A. Hellwing, Y. Hoffman, B. J. T. Jones, F. Kitaura, A. Knebe, S. Manti, M. Neyrinck, S. E. Nuza, N. Padilla, E. Platen, N. Ramachandra, A. Robotham, E. Saar, S. Shand arin, M. Steinmetz, R. S. Stoica, T. Sousbie, and G. Yepes. Tracing the cosmic web. , 473(1):1195–1217, Jan. 2018. doi: 10.1093/mnras/stx1976.

NASA. New hubble constant adds to mistery of universe's expansion rate, a. URL https://hubblesite.org/contents/news-releases/2019/news-2019-28.

NASA. How fast is the universe expansing?, b. URL https://wmap.gsfc.nasa.gov/universe/uni_expansion.html.

NOVA. Can we a-void the hubble tension with local voids? URL https://aasnova.org/2019/03/05/can-we-a-void-the-hubble-tension-with-local-voids/.

R. Panek. A cosmic crisis. *Scientific American*, 322:30–37, March 2020. doi: 10.1038/scientificamerican0320-30.

Planck Collaboration, N. Aghanim, Y. Akrami, M. Ashdown, J. Aumont, C. Baccigalupi, M. Ballardini, A. J. Banday, R. B. Barreiro, N. Bartolo, S. Basak, R. Battye, K. Benabed, J. P. Bernard, M. Bersanelli, P. Bielewicz, J. J. Bock, J. R. Bond, J. Borrill, F. R. Bouchet, F. Boulanger, M. Bucher, C. Burigana, R. C. Butler, E. Calabrese, J. F. Cardoso, J. Carron, A. Challinor, H. C. Chiang, J. Chluba, L. P. L. Colombo, C. Combet, D. Contreras, B. P. Crill, F. Cuttaia, P. de Bernardis, G. de Zotti, J. Delabrouille, J. M. Delouis, E. Di Valentino, J. M. Diego, O. Doré, M. Douspis, A. Ducout, X. Dupac, S. Dusini, G. Efstathiou, F. Elsner, T. A. Enßlin, H. K. Eriksen, Y. Fantaye, M. Farhang, J. Fergusson, R. Fernandez-Cobos, F. Finelli, F. Forastieri, M. Frailis, A. A. Fraisse, E. Franceschi, A. Frolov, S. Galeotta, S. Galli, K. Ganga, R. T. Génova-Santos, M. Gerbino,

T. Ghosh, J. González-Nuevo, K. M. Górski, S. Gratton, A. Gruppuso, J. E. Gudmundsson, J. Hamann, W. Handley, F. K. Hansen, D. Herranz, S. R. Hildebrandt, E. Hivon, Z. Huang, A. H. Jaffe, W. C. Jones, A. Karakci, E. Keihänen, R. Keskitalo, K. Kiiveri, J. Kim, T. S. Kisner, L. Knox, N. Krachmalnicoff, M. Kunz, H. Kurki-Suonio, G. Lagache, J. M. Lamarre, A. Lasenby, M. Lattanzi, C. R. Lawrence, M. Le Jeune, P. Lemos, J. Lesgourgues, F. Levrier, A. Lewis, M. Liguori, P. B. Lilje, M. Lilley, V. Lindholm, M. López-Caniego, P. M. Lubin, Y. Z. Ma, J. F. Macías-Pérez, G. Maggio, D. Maino, N. Mandolesi, A. Mangilli, A. Marcos-Caballero, M. Maris, P. G. Martin, M. Martinelli, E. Martínez-González, S. Matarrese, N. Mauri, J. D. McEwen, P. R. Meinhold, A. Melchiorri, A. Mennella, M. Migliaccio, M. Millea, S. Mitra, M. A. Miville-Deschênes, D. Molinari, L. Montier, G. Morgante, A. Moss, P. Natoli, H. U. Nørgaard-Nielsen, L. Pagano, D. Paoletti, B. Partridge, G. Patanchon, H. V. Peiris, F. Perrotta, V. Pettorino, F. Piacentini, L. Polastri, G. Polenta, J. L. Puget, J. P. Rachen, M. Reinecke, M. Remazeilles, A. Renzi, G. Rocha, C. Rosset, G. Roudier, J. A. Rubiño-Martín, B. Ruiz-Granados, L. Salvati, M. Sandri, M. Savelainen, D. Scott, E. P. S. Shellard, C. Sirignano, G. Sirri, L. D. Spencer, R. Sunyaev, A. S. Suur-Uski, J. A. Tauber, D. Tavagnacco, M. Tenti, L. Toffolatti, M. Tomasi, T. Trombetti, L. Valenziano, J. Valiviita, B. Van Tent, L. Vibert, P. Vielva, F. Villa, N. Vittorio, B. D. Wand elt, I. K. Wehus, M. White, S. D. M. White, A. Zacchei, and A. Zonca. Planck 2018 results. VI. Cosmological parameters. *arXiv e-prints*, art. arXiv:1807.06209, July 2018.

A. G. Reiss. A 2.4% determination of the local value of the hubble constant. *2016. The American Astronomical Society*, 826, July 2016. doi: 10.3847/0004-637X/826/1/56.

A. G. Riess, S. Casertano, W. Yuan, L. M. Macri, and D. Scolnic. Large Magellanic Cloud Cepheid Standards Provide a 1% Foundation for the Determination of the Hubble Constant and Stronger Evidence for Physics beyond ΛCDM. , 876(1):85, May 2019. doi: 10.3847/1538-4357/ab1422.

B. Ryden. *Introduction to Cosmology*. Cambridge University Press, 2016.

R. Sheth and R. van de Weygaert. A hierarchy of voids: Much ado about nothing. *Monthly Notices of the Royal Astronomical Society*, 350, 12 2003. doi: 10.1111/j.1365-2966.2004.07661.x.

R. van de Weygaert. Voids and the cosmic web: cosmic depression & spatial complexity. *Proceedings of the International Astronomical Union*, 11:493–523, 06 2014. doi: 10.1017/S1743921316010504.

R. van de Weygaert and J. Bond. Observations and morphology of the cosmic web. *Lecture Notes in Physics*, 740, 01 2008. doi: 10.1007/978-1-4020-6941-3_11.

R. van de Weygaert and E. Platen. Cosmic Voids: Structure, Dynamics and Galaxies. In *International Journal of Modern Physics Conference Series*, volume 1 of *International Journal of Modern Physics Conference Series*, pages 41–66, Jan. 2011. doi: 10.1142/S2010194511000092.

L. Verde, T. Treu, and A. G. Riess. Tensions between the early and late Universe. *Nature Astronomy*, 3:891–895, Sept. 2019. doi: 10.1038/s41550-019-0902-0.

S. Watson. An exposition on inflationary cosmology. 04 2000.

R. Weygaert. Fragmenting the universe. 3: The constructions and statistics of 3-d voronoi tessellations. *Astronomy and Astrophysics*, 283:361–406, 02 1994.

K. C. Wong, S. H. Suyu, G. C. F. Chen, C. E. Rusu, M. Millon, D. Sluse, V. Bonvin, C. D. Fassnacht, S. Taubenberger, M. W. Auger, S. Birrer, J. H. H. Chan, F. Courbin, S. Hilbert, O. Tihhonova, T. Treu, A. Agnello, X. Ding, I. Jee, E. Komatsu, A. J. Shajib, A. Sonnenfeld, R. D. Bland ford, L. V. E. Koopmans, P. J. Marshall, and G. Meylan. H0LiCOW XIII. A 2.4% measurement of H_0 from lensed quasars: 5.3σ tension between early and late-Universe probes. , June 2020. doi: 10.1093/mnras/stz3094.

H.-Y. Wu and D. Huterer. Sample variance in the local measurements of the Hubble constant. *Monthly Notices of the Royal Astronomical Society*, 471 (4):4946–4955, 08 2017. ISSN 0035-8711. doi: 10.1093/mnras/stx1967. URL `https://doi.org/10.1093/mnras/stx1967`.

C. Y. Yau and J. M. Loh. A generalization of the neyman-scott process. *Statistica Sinica*, 22, 10 2012. doi: 10.5705/ss.2010.245.